

Ultralight dark matter detection with levitated ferromagnets

Saarik Kalia,^{1,*} Dmitry Budker,^{2,3,4} Derek F. Jackson Kimball,⁵ Wei Ji,^{2,3} Zhen Liu,¹ Alexander O. Sushkov,^{6,7,8,9} Chris Timberlake,¹⁰ Hendrik Ulbricht,¹⁰ Andrea Vinante,^{11,12} and Tao Wang¹³

¹*School of Physics & Astronomy, University of Minnesota, Minneapolis, MN 55455, USA*

²*Johannes Gutenberg University Mainz, 55128 Mainz, Germany*

³*Helmholtz-Institute, GSI Helmholtzzentrum für Schwerionenforschung, 55128 Mainz, Germany*

⁴*Department of Physics, University of California at Berkeley, Berkeley, California 94720-7300, USA*

⁵*Department of Physics, California State University – East Bay, Hayward, CA 94542, USA*

⁶*Department of Physics, Boston University, Boston, MA 02215, USA*

⁷*Department of Electrical and Computer Engineering, Boston University, Boston, MA 02215, USA*

⁸*Photonics Center, Boston University, Boston, MA 02215, USA*

⁹*Department of Physics & Astronomy, The Johns Hopkins University, Baltimore, MD 21218, USA*

¹⁰*School of Physics and Astronomy, University of Southampton, Southampton SO17 1BJ, UK*

¹¹*Istituto di Fotonica e Nanotecnologie IFN-CNR, 38123 Povo, Trento, Italy*

¹²*Fondazione Bruno Kessler (FBK), 38123 Povo, Trento, Italy*

¹³*A*STAR Quantum Innovation Centre (Q.InC),*

Institute of Materials Research and Engineering (IMRE),

*Agency for Science, Technology and Research (A*STAR),*

2 Fusionopolis Way, 08-03, Singapore, 138634, Republic of Singapore

(Dated: August 29, 2024)

Levitated ferromagnets act as ultraprecise magnetometers, which can exhibit high quality factors due to their excellent isolation from the environment. These instruments can be utilized in searches for ultralight dark matter candidates, such as axionlike dark matter or dark-photon dark matter. In addition to being sensitive to an axion-photon coupling or kinetic mixing, which produce physical magnetic fields, ferromagnets are also sensitive to the effective magnetic field (or “axion wind”) produced by an axion-electron coupling. While the dynamics of a levitated ferromagnet in response to a DC magnetic field have been well studied, all of these couplings would produce AC fields. In this work, we study the response of a ferromagnet to an applied AC magnetic field and use these results to project their sensitivity to axion and dark-photon dark matter. We pay special attention to the direction of motion induced by an applied AC field, in particular, whether it precesses around the applied field (similar to an electron spin) or librates in the plane of the field (similar to a compass needle). We show that existing levitated ferromagnet setups can already have comparable sensitivity to an axion-electron coupling as comagnetometer or torsion balance experiments. In addition, future setups can become sensitive probes of axion-electron coupling, dark-photon kinetic mixing, and axion-photon coupling, for ultralight dark matter masses $m_{\text{DM}} \lesssim \text{feV}$.

I. INTRODUCTION

Levitated ferromagnets can serve as excellent instruments for precision measurements of torques and magnetic fields [1–5], which can be applied to tests of fundamental physics and searches for new physics [6, 7]. Due to the intrinsic spin of its polarized electrons, a ferromagnet may act as a gyroscope in the limit where the spin contribution $S = N\hbar/2$ to its total angular momentum dominates over the contribution from its rotational angular momentum $L = I\omega$ [1].¹ In such a case, the ferromagnet will precess around an applied DC magnetic field, similar to a single electron spin. In the opposite limit $S \ll L$, the dominant motion of the ferromagnet will be to librate in the plane of the applied field, similar to a compass needle.

In order to realize the potential of this system, the ferromagnet must be adequately isolated from its environment. One of the most promising ways is to levitate the ferromagnet over a superconducting plane [3–6, 8]. In such a scenario, the ferromagnet is repelled by an “image” magnetic dipole located below the plane. The presence of this superconducting plane can significantly affect the dynamics of the ferromagnet, slowing down its precession frequency.² Alternatively, it has been proposed to place the ferromagnet in freefall [7], in order to avoid

* kalias@umn.edu

¹ Generically, this is a tensor relation. For simplicity, here we assume the moment of inertia tensor I is diagonal; see also discussion following Eq. (7).

² As discussed in Ref. [6], a ferromagnet levitated above a superconducting surface by the Meissner effect possesses cylindrical symmetry and thus conserves the angular momentum component along the direction \hat{z} perpendicular to the superconducting surface. If such a levitated ferromagnet experiences a torque that would cause it to precess, in order to conserve angular momentum along z , the ferromagnet must tilt such that its spin component S_z , counteracts the rotational angular momentum component L_z induced by the precession. This in turn tilts the image dipole in such a way as to suppress the torque experienced by the ferromagnet, thereby suppressing the precession frequency. This effect can suppress the precession frequency by

the effects of any trapping potential.

One particularly interesting application of levitated ferromagnets is the search for ultralight dark matter candidates, including axion and axion-like dark matter (henceforth, simply axion DM) and dark-photon dark matter (DPDM). The former can address the strong-CP problem [9–11], while both can exhibit the correct relic abundance [12–16] and generically arise in new physics theories of many different origins, see, e.g., a recent review [17]. In the ultralight regime, these candidates behave as classical fields, which oscillate near their Compton frequencies [18, 19]. Axion DM could potentially couple to electron spins, causing them to precess, as if it were an AC magnetic field [20–22]. As a ferromagnet is composed of many polarized electrons, axion DM can impart a collective oscillating torque on the whole ferromagnet. In addition, axion DM and DPDM can both couple to photons, generating a physical AC magnetic field, which could also impart a torque on a ferromagnet.

While the response of a ferromagnet to an applied DC magnetic field has been well studied, both in freefall and above a superconductor [1, 6], the response to a driving AC magnetic field has not been adequately addressed thus far.

The purpose of this work is to study the dynamics of a ferromagnet in response to an AC magnetic field and to apply these dynamics to the case of ultralight DM. In Sec. II, we derive the response of the system to an applied AC magnetic field, which is qualitatively different from the DC case. This is because, in the DC case, the precession frequency is given by the Larmor frequency, which is proportional to the applied magnetic field. Meanwhile, we will see that in the AC case, the frequency of the ferromagnet dynamics is determined by the frequency of the AC field (the Compton frequency, in the case of ultralight DM). Therefore, whether the ferromagnet precesses as a gyroscope or librates as a compass needle will be frequency-dependent. Moreover, as mentioned above, the presence of a levitation/trapping mechanism can alter the dynamics of the system. We will determine in what contexts the ferromagnet undergoes precession vs. libration.

In Sec. III, we compute the sensitivity of a ferromagnet to an applied AC magnetic field. We review the relevant noise sources and utilize the results of Sec. II to determine the magnetic-field sensitivity of a ferromagnet setup, accounting for motion in both angular directions. We propose three cases of interest: one representative of an existing levitated setup [5], a future levitated setup, and a future freefall setup. The parameter choices for these setups are shown in Tab. I and their magnetic-field sensitivities are computed in Fig. 5.

In Sec. IV, we project the sensitivities of these setups to ultralight DM. We review the physics of axion DM

coupled to electrons, kinetically mixed DPDM, and axion DM coupled to photons. In each case, we compute the effective/physical AC magnetic field generated by the DM candidate, and show the sensitivities of the three setups of interest to the DM candidate in Fig. 6.

In Sec. V, we conclude. We make all the code used in this work publicly available on Github [23].

II. LEVITATED FERROMAGNETS

In this section, we compute the response of a levitated ferromagnet to an applied AC magnetic field. Importantly, we account for the effect of any trapping potential on the ferromagnet’s response and determine when libration versus precession occurs. We begin by introducing some examples of trapping potentials. Then, we derive the equations of motion for the dynamics of the ferromagnet in this trap. Finally, we show how these dynamics are modified in the presence of a driving field.

A. Trapping potential

Generically, in order for the ferromagnet to remain levitated, it must be trapped in both the translational and angular directions. In other words, it must sit at the minimum $(\mathbf{x}_0, \hat{\mathbf{n}}_0)$ of some potential $V(\mathbf{x}, \hat{\mathbf{n}})$. Here \mathbf{x} denotes the position of the ferromagnet, while $\hat{\mathbf{n}} = (\theta, \phi)$ describes its orientation (using spherical coordinates with $\theta = 0$ the positive z -axis). In this work, we will consider the magnetic moment of the ferromagnet to be locked to its spatial orientation so that $\hat{\mathbf{n}}$ more specifically denotes the direction of its magnetic moment.³ If the ferromagnet consists of N polarized electron spins, then its magnetic moment is given by

$$\boldsymbol{\mu} = -\gamma_e \mathbf{S} \equiv -\gamma_e \cdot \frac{N\hbar}{2} \hat{\mathbf{n}}, \quad (1)$$

where $\gamma_e = g_e \mu_B / \hbar$ is the electron gyromagnetic ratio. (g_e is the electron g -factor and $\mu_B = e\hbar/2m_e$ is the Bohr magneton.)

There are various ways in which the ferromagnet can be trapped in a potential. Perhaps the simplest is to levitate the ferromagnet in some static magnetic field $\mathbf{B}(\mathbf{x})$.

³ In general, the individual electron spins \mathbf{S}_i within the ferromagnet are not locked to its orientation $\hat{\mathbf{n}}$. The atomic lattice of the ferromagnet exhibits some interaction with each electron spin, which relaxes the spins to align with the lattice. This relaxation occurs at a typical rate $\Gamma \sim \text{GHz}$ [24]. In this work, we only consider dynamics at much lower frequencies than this, and so it is safe to treat the macroscopic magnetic moment of the ferromagnet to be locked to its orientation. We do note that coupling of individual spin fluctuations to external magnetic fields can act as an additional noise source, though this noise is typically small [25].

orders of magnitude for ferromagnets with characteristic sizes above ~ 0.1 microns.

This gives the trapping potential

$$V(\mathbf{x}, \hat{\mathbf{n}}) = -\boldsymbol{\mu} \cdot \mathbf{B}(\mathbf{x}) + mgz, \quad (2)$$

where the latter term arises due to gravity (m is the mass of the ferromagnet, and g is the gravitational acceleration on Earth). In such a potential, the ferromagnet will always prefer to align with the local magnetic field, i.e. $\hat{\mathbf{n}}_0 = \hat{\mathbf{B}}(\mathbf{x}_0)$.⁴ Note that in this case, the ferromagnet will, in general, be trapped in both angular directions, i.e. $\partial_\theta^2 V, \partial_\phi^2 V \Big|_{(\mathbf{x}_0, \hat{\mathbf{n}}_0)} > 0$.⁵

Alternatively, the ferromagnet may be levitated above a superconducting plane. The potential in such a setup can be computed via the method of images; that is, if the ferromagnet lies a distance z above the superconducting plane, then one computes the potential it feels due to a magnetic moment located a distance z below the superconducting plane [4, 6]. This gives a potential⁶

$$V(\mathbf{x}, \hat{\mathbf{n}}) = -\frac{1}{2} \boldsymbol{\mu} \cdot \frac{\mu_0}{4\pi} \frac{3(\tilde{\mathbf{x}} \cdot \tilde{\boldsymbol{\mu}})\tilde{\mathbf{x}} - \tilde{x}^2 \tilde{\boldsymbol{\mu}}}{\tilde{x}^5} + mgz \quad (3)$$

$$= \frac{\mu_0 \mu^2}{64\pi z^3} (1 + \cos^2 \theta) + mgz, \quad (4)$$

where $\tilde{\mathbf{x}} = 2z\hat{\mathbf{z}}$ is the distance between the ferromagnet and its image, and $\tilde{\boldsymbol{\mu}} = (\pi - \theta, \phi)$ is the orientation of the image magnetic moment. It is clear in this case that the ferromagnet is trapped in the θ -direction, with its minimum at $\theta_0 = \pi/2$ (parallel to the superconducting plane), but it is free to rotate in the ϕ -direction. In a physical system, this exact degeneracy in the ϕ -direction will be broken, but nevertheless, the trapping in the ϕ -direction can be significantly weaker than the trapping in the θ -direction, i.e. $\partial_\theta^2 V \Big|_{(\mathbf{x}_0, \hat{\mathbf{n}}_0)} \gg \partial_\phi^2 V \Big|_{(\mathbf{x}_0, \hat{\mathbf{n}}_0)}$.

B. Ferromagnet dynamics

Now let us derive the equations of motion for the ferromagnet. We will first consider only the trapping potential, without the presence of any driving AC magnetic

⁴ By Earnshaw's theorem, a static magnetic field alone cannot stably levitate a magnetic dipole [26]. The equilibrium \mathbf{x}_0 can be made stable through an active feedback loop, a method known as electromagnetic levitation [27]. In this work, we focus primarily on the angular motion of the ferromagnet, and so do not worry about the stability of the translational modes.

⁵ We note that this spherical coordinate system becomes pathological when $\hat{\mathbf{n}}_0 = \hat{\mathbf{z}}$ because ϕ is not well-defined at this point. In the sections that follow, we will consider only the angular dependence of $V(\hat{\mathbf{n}})$, in which case we will be free to rotate our coordinate system so that $\hat{\mathbf{n}}_0 \neq \hat{\mathbf{z}}$.

⁶ Note the additional factor of $\frac{1}{2}$ in the first term of Eq. (3). Without this factor, this term would describe the work required to bring two physical dipoles from infinity to a distance $2z$ apart. Because we have only one physical dipole, only half the work is required to bring it to a distance $2z$ from its image.

field. In the remainder of this work, we will also ignore translational motion, and only focus on the angular dependence of $V(\hat{\mathbf{n}})$.⁷ Let the total angular momentum of the ferromagnet be given by $\mathbf{J} = \mathbf{S} + \mathbf{L}$, which consists of both an intrinsic spin contribution \mathbf{S} and an orbital angular momentum contribution \mathbf{L} . The potential exerts a torque

$$\boldsymbol{\tau} = \frac{\partial \mathbf{J}}{\partial t} = -\hat{\mathbf{n}} \times \nabla_{\hat{\mathbf{n}}} V \quad (5)$$

$$\equiv -\hat{\mathbf{n}} \times \left(\frac{\partial V}{\partial \theta} \hat{\boldsymbol{\theta}} + \frac{1}{\sin \theta} \frac{\partial V}{\partial \phi} \hat{\boldsymbol{\phi}} \right) \quad (6)$$

on the ferromagnet. Additionally, the orientation of the ferromagnet rotates around its orbital angular momentum

$$\frac{\partial \hat{\mathbf{n}}}{\partial t} = \boldsymbol{\Omega} \times \hat{\mathbf{n}} = (I^{-1} \mathbf{L}) \times \hat{\mathbf{n}}. \quad (7)$$

Generically, the moment of inertia I may be an anisotropic tensor. However, for simplicity, in this work, we will take I to be diagonal, e.g., in the case of a spherical ferromagnet. Note that because $\mathbf{S} \propto \hat{\mathbf{n}}$, then we may replace \mathbf{L} in this expression with \mathbf{J} . If we make this replacement, then these two equations of motion govern the dynamics of $\hat{\mathbf{n}}$ and \mathbf{J} . Let us normalize all of our quantities by the intrinsic spin

$$\mathbf{J} = \frac{N\hbar}{2} \mathbf{j} \quad (8)$$

$$\mathbf{L} = \frac{N\hbar}{2} \boldsymbol{\ell} \quad (9)$$

$$\omega_I = \frac{N\hbar}{2I} \quad (10)$$

$$V = \frac{N\hbar}{2} v, \quad (11)$$

so that we may rewrite the equations of motion Eq. (5) and (7) as

$$\frac{\partial \mathbf{j}}{\partial t} = -\hat{\mathbf{n}} \times \nabla_{\hat{\mathbf{n}}} v \quad (12)$$

$$\frac{\partial \hat{\mathbf{n}}}{\partial t} = \omega_I (\mathbf{j} \times \hat{\mathbf{n}}). \quad (13)$$

The frequency ω_I is known as the Einstein-de Haas frequency [28].

⁷ The translational modes of the system will not be directly excited by a uniform magnetic field but instead can only be excited by a magnetic field gradient. The DM models of interest and the frequency regime considered in this work produce magnetic-field signals that are relatively uniform, so in this work, we will neglect any such gradients. In principle, the translational modes may also exhibit some coupling to the angular modes, e.g. due to inhomogeneities in the trap. This cross-coupling is small in existing experiments [3, 4].

Let us decompose these equations of motion in terms of the unit vectors $\hat{\mathbf{n}}$, $\hat{\boldsymbol{\theta}}$, and $\hat{\boldsymbol{\phi}}$ in spherical coordinates. The time derivatives of these coordinates are related by

$$\frac{\partial \hat{\mathbf{n}}}{\partial t} = \frac{\partial \theta}{\partial t} \hat{\boldsymbol{\theta}} + \sin \theta \frac{\partial \phi}{\partial t} \hat{\boldsymbol{\phi}} \quad (14)$$

$$\frac{\partial \hat{\boldsymbol{\theta}}}{\partial t} = -\frac{\partial \theta}{\partial t} \hat{\mathbf{n}} + \cos \theta \frac{\partial \phi}{\partial t} \hat{\boldsymbol{\phi}} \quad (15)$$

$$\frac{\partial \hat{\boldsymbol{\phi}}}{\partial t} = -\sin \theta \frac{\partial \phi}{\partial t} \hat{\mathbf{n}} - \cos \theta \frac{\partial \phi}{\partial t} \hat{\boldsymbol{\theta}}, \quad (16)$$

and the total angular momentum \mathbf{j} can be decomposed as

$$\mathbf{j} = j_n \hat{\mathbf{n}} + j_\theta \hat{\boldsymbol{\theta}} + j_\phi \hat{\boldsymbol{\phi}}. \quad (17)$$

Note that Eq. (12) and Eq. (13) imply

$$\frac{\partial j_n}{\partial t} = \mathbf{j} \cdot \frac{\partial \hat{\mathbf{n}}}{\partial t} + \frac{\partial \mathbf{j}}{\partial t} \cdot \hat{\mathbf{n}} = 0, \quad (18)$$

so that j_n is a constant of motion. If the ferromagnet is not spinning around its magnetic moment axis, then the orbital angular momentum $\boldsymbol{\ell}$ has no component along $\hat{\mathbf{n}}$, and so $j_n = 1$. In the interest of maintaining generality, we will leave our results in terms of j_n . As we will see in Sec. II C, the limit $j_n \rightarrow 0$ will correspond to the “compass” behavior where the ferromagnet’s angular momentum is dominated by its orbital angular momentum, while the limit $j_n \rightarrow \infty$ will correspond to the “electron

spin” behavior where it is dominated by its intrinsic angular momentum.

In terms of our spherical-coordinate variables, Eq. (12) and Eq. (13) become

$$\frac{\partial j_\theta}{\partial t} - j_\phi \cos \theta \frac{\partial \phi}{\partial t} + j_n \frac{\partial \theta}{\partial t} = \frac{1}{\sin \theta} \frac{\partial v}{\partial \phi} \quad (19)$$

$$\frac{\partial j_\phi}{\partial t} + j_\theta \cos \theta \frac{\partial \phi}{\partial t} + j_n \sin \theta \frac{\partial \phi}{\partial t} = -\frac{\partial v}{\partial \theta} \quad (20)$$

$$\frac{\partial \theta}{\partial t} = \omega_I j_\phi \quad (21)$$

$$\sin \theta \frac{\partial \phi}{\partial t} = -\omega_I j_\theta. \quad (22)$$

These can then be combined to give

$$\frac{\partial^2 \theta}{\partial t^2} - \frac{\sin 2\theta}{2} \left(\frac{\partial \phi}{\partial t} \right)^2 + j_n \omega_I \sin \theta \frac{\partial \phi}{\partial t} + \omega_I \frac{\partial v}{\partial \theta} = 0 \quad (23)$$

$$\sin^2 \theta \frac{\partial^2 \phi}{\partial t^2} + \sin 2\theta \frac{\partial \phi}{\partial t} \frac{\partial \theta}{\partial t} - j_n \omega_I \sin \theta \frac{\partial \theta}{\partial t} + \omega_I \frac{\partial v}{\partial \phi} = 0. \quad (24)$$

Finally, let us suppose that the motion of the ferromagnet is small⁸, so that we may perturb Eq. (23) and Eq. (24) around the minimum $\hat{\mathbf{n}}_0 = (\theta_0, \phi_0)$ of v . Namely, let us write $\theta = \theta_0 + \delta\theta$ and $\phi = \phi_0 + \delta\phi$. Then to first order, these equations become

$$\left[\partial_t^2 \begin{pmatrix} 1 & 0 \\ 0 & \sin^2 \theta_0 \end{pmatrix} + j_n \omega_I \sin \theta_0 \partial_t \begin{pmatrix} 0 & 1 \\ -1 & 0 \end{pmatrix} + \omega_I \begin{pmatrix} v_{\theta\theta} & v_{\theta\phi} \\ v_{\phi\theta} & v_{\phi\phi} \end{pmatrix} \right] \begin{pmatrix} \delta\theta \\ \delta\phi \end{pmatrix} = 0, \quad (25)$$

where $v_{\alpha\beta} = \partial_\alpha \partial_\beta v|_{(\theta_0, \phi_0)}$.

C. Response to AC magnetic field

Eq. (25) encodes all the important dynamics of the ferromagnet. To understand the structure of this equation, let us consider the effect of an AC magnetic field $\mathbf{B}(t) = \mathbf{B}_0 \cos \omega t$ on the ferromagnet.⁹ This magnetic

field will have the same effect as a (time-dependent) potential of the form of the first term in Eq. (2). If we write

$$\mathbf{B}_0 = B_0 \hat{\mathbf{b}} = B_0 \left(b_n \hat{\mathbf{n}}_0 + b_\theta \hat{\boldsymbol{\theta}}_0 + b_\phi \hat{\boldsymbol{\phi}}_0 \right) \quad (26)$$

in terms of the spherical-coordinate unit vectors at (θ_0, ϕ_0) , then this corresponds to a normalized potential

$$v_B(\theta_0 + \delta\theta, \phi_0 + \delta\phi, t) = \omega_L \cos \omega t \left(\hat{\mathbf{n}} \cdot \hat{\mathbf{b}} \right) \quad (27)$$

$$\approx \omega_L \cos \omega t (b_n + b_\theta \delta\theta + b_\phi \sin \theta_0 \delta\phi) \quad (28)$$

where $\omega_L = \gamma_e B_0$. Plugging v_B into Eq. (23) and Eq. (24) as an additional contribution to v , we find that it acts as an AC driving force for the system (because $\partial_\theta v_B, \partial_\phi v_B \neq 0$). In particular, it will appear on the

⁸ as the dark matter signal we consider in the weakly coupled case generates a small, oscillating perturbation to the system

⁹ In this subsection, we will assume that the AC magnetic field is linearly polarized. This is because we will be interested in distinguishing whether the ferromagnet librates or precesses, and such a notion is only well-defined if the direction of the field is fixed. This will be the case for an axion-wind signal $\mathbf{B}_{ae} \sim \nabla a$ [see Eq. (67)], since all components of the gradient are in-phase. This will, however, not be the case for a DPDM signal, as the components of the dark photon may have different phases

[see Eq. (74)], and so the resulting magnetic-field signal may be elliptically polarized.

right-hand side of Eq. (25) as

$$-\omega_I \omega_L \cos \omega t \begin{pmatrix} b_\theta \\ b_\phi \sin \theta_0 \end{pmatrix}. \quad (29)$$

We can then readily interpret the structure of Eq. (25). The first row represents how the system responds to an applied magnetic field in the θ -direction, while the second row represents how the system responds to an applied magnetic field in the ϕ -direction. Meanwhile, the first column represents motion in the θ -direction, and the second column represents motion in the ϕ -direction. This tells us that the diagonal elements of Eq. (25) in-

dicate libration, while the off-diagonal elements indicate precession!

Let us now analyze the behavior of this system in various cases. Without loss of generality, we may orient our coordinates so that $\theta_0 = \frac{\pi}{2}$, $\phi_0 = 0$, and $v_{\theta\phi} = v_{\phi\theta} = 0$. Moreover, let us complexify the AC magnetic field $\mathbf{B}(t) = \mathbf{B}_0 e^{-i\omega t}$. The homogeneous response of $\delta\theta$ and $\delta\phi$ will then be

$$\begin{pmatrix} \delta\theta \\ \delta\phi \end{pmatrix} = -\frac{N\hbar\gamma_e B_0}{2} \cdot \chi(\omega) \begin{pmatrix} b_\theta \\ b_\phi \end{pmatrix}, \quad (30)$$

where the mechanical susceptibility $\chi(\omega)$ is given by

$$\chi(\omega)^{-1} = I \left[-\omega^2 \begin{pmatrix} 1 & 0 \\ 0 & 1 \end{pmatrix} - ij_n \omega_I \omega \begin{pmatrix} 0 & 1 \\ -1 & 0 \end{pmatrix} + \omega_I \begin{pmatrix} v_{\theta\theta} & 0 \\ 0 & v_{\phi\phi} \end{pmatrix} \right]. \quad (31)$$

We will consider a few properties of the system based on the characteristics of $\chi(\omega)$. Firstly, we will be interested in the resonances of the system, which occur at the frequencies where $\chi(\omega)^{-1}$ becomes singular. Secondly, we will determine whether libration or precession dominates the motion, based on whether the off-diagonal components of χ are larger than its diagonal components.¹⁰ Finally, we will consider the behavior of the sensitivity as a function of frequency ω . As shown in Appendix A, the peak sensitivity of the system is primarily determined by the eigenvalue of χ with the largest absolute value $\lambda_{\max}(\omega)$. We consider three cases of interest for this system (without loss of generality, we take $v_{\theta\theta} \gg v_{\phi\phi}$ in all three cases, but their roles will simply be interchanged if the hierarchy is flipped):

- **Trapped** ($v_{\theta\theta}/j_n \gg v_{\phi\phi}/j_n \gg j_n \omega_I$): This will be the case, for instance, when the ferromagnet is trapped by a strong magnetic field, as in Eq. (2). At all frequencies, the second term in Eq. (31) can be neglected, and so the dominant motion is libration. The system exhibits two resonances at $\omega \approx \sqrt{\omega_I v_{\theta\theta}}$ and $\omega \approx \sqrt{\omega_I v_{\phi\phi}}$. For $\omega \ll \sqrt{\omega_I v_{\phi\phi}}$, the response of the system is flat as a function of ω , that is $\lambda_{\max}(\omega) \approx (I\omega_I v_{\phi\phi})^{-1}$. Meanwhile for $\omega \gg \sqrt{\omega_I v_{\phi\phi}}$, it decays as $|\lambda_{\max}(\omega)| \approx I^{-1} \omega^{-2}$ (except near the resonance $\omega \approx \sqrt{\omega_I v_{\theta\theta}}$).

¹⁰ One may wonder whether this definition of libration/precession is coordinate-dependent. Because we have assumed $\mathbf{B}(t)$ is linearly polarized (see footnote 9), then b_θ and b_ϕ are real, and so we should restrict our coordinate transformations to be orthogonal (as opposed to unitary). Given any 2×2 Hermitian matrix, an orthogonal transformation can always be performed so that the off-diagonal components become purely imaginary. This coordinate choice minimizes the size of the off-diagonal components, and libration/precession can always be defined in these coordinates. The matrix in Eq. (31) is conveniently already in these coordinates, so we require no transformation.

• **Partially trapped** ($v_{\theta\theta}/j_n \gg j_n \omega_I \gg v_{\phi\phi}/j_n$): This will be the case, for instance, when the ferromagnet is trapped above a superconductor, as in Eq. (4) [and the degeneracy in the ϕ -direction is only weakly broken]. The resonant frequencies are again $\omega \approx \sqrt{\omega_I v_{\theta\theta}}$ and $\omega \approx \sqrt{\omega_I v_{\phi\phi}}$. The off-diagonal components of Eq. (31) are always subdominant to the $\theta\theta$ -component, however, for $j_n \omega_I \gg \omega \gg v_{\phi\phi}/j_n$, they are larger than the $\phi\phi$ -component. This implies that in this frequency range, an AC magnetic field in the ϕ -direction will result in libration, while one in the θ -direction will result in precession. The behavior of λ_{\max} is the same as in the trapped case. We note that in the frequency range where precession can occur, the eigenvector associated with λ_{\max} is closely aligned with the ϕ -direction. Therefore even though precession can be achieved, it is not the dominant behavior of the system.

• **Gyroscope** ($j_n \omega_I \gg v_{\theta\theta}/j_n \gg v_{\phi\phi}/j_n$): This will be the case, for instance, when the ferromagnet is in (near) freefall. The resonant frequencies are now $\omega \approx \omega_I$ and $\omega \approx \sqrt{v_{\theta\theta} v_{\phi\phi}}$. When $j_n \omega_I \gg \omega \gg v_{\theta\theta}/j_n$, the off-diagonal components dominate, and there is precession in both directions. When $v_{\theta\theta}/j_n \gg \omega \gg v_{\phi\phi}/j_n$, there will be precession in one direction and libration in the other. For all other frequencies, there will only be libration. The response of such a system as a function of frequency is given by

$$|\lambda_{\max}(\omega)| \approx \begin{cases} (I\omega_I v_{\phi\phi})^{-1}, & \omega \ll \sqrt{v_{\theta\theta} v_{\phi\phi}}/j_n \\ v_{\theta\theta}/(j_n^2 I\omega_I \omega^2), & v_{\theta\theta}/j_n \gg \omega \gg \sqrt{v_{\theta\theta} v_{\phi\phi}}/j_n \\ (Ij_n \omega_I \omega)^{-1}, & j_n \omega_I \gg \omega \gg v_{\theta\theta}/j_n \\ I^{-1} \omega^{-2}, & \omega \gg j_n \omega_I. \end{cases} \quad (32)$$

In Figs. 1 and 2, we show the behavior of χ in the “par-

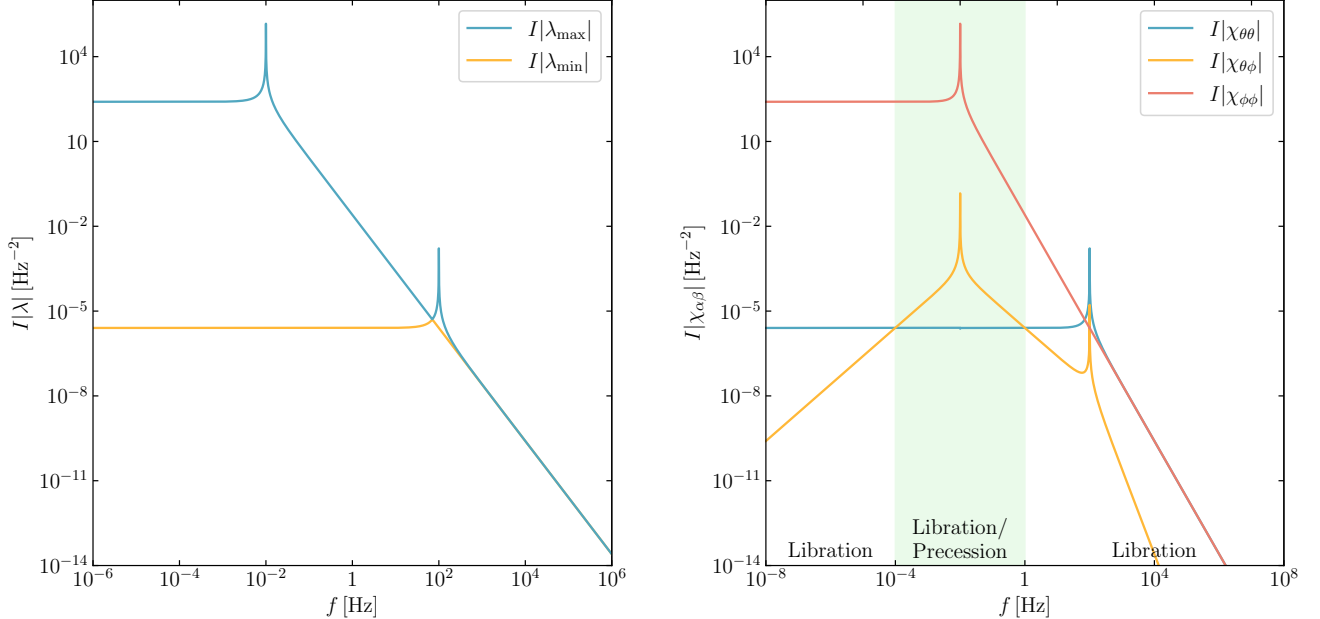


FIG. 1. Absolute values of the eigenvalues (left) and elements (right) of $\chi(\omega)$ in the “partially trapped” case. In these plots, we set $v_{\theta\theta} = 2\pi \cdot 10^4$ Hz, $\omega_I = 2\pi \cdot 1$ Hz, $v_{\phi\phi} = 2\pi \cdot 10^{-4}$ Hz, and $j_n = 1$. On the left, the blue line denotes the larger eigenvalue, which predominantly determines the sensitivity of the system, while the orange line denotes the smaller eigenvalue. Note that the larger eigenvalue exhibits resonances at $\omega = \sqrt{\omega_I v_{\phi\phi}}$ and $\omega = \sqrt{\omega_I v_{\theta\theta}}$. On the right, the blue, orange, and red lines represent $I|\chi_{\theta\theta}|$, $I|\chi_{\theta\phi}|$, and $I|\chi_{\phi\phi}|$, respectively. Note that $|\chi_{\theta\phi}| > |\chi_{\theta\theta}|$ for $j_n \omega_I \gg \omega \gg v_{\phi\phi}/j_n$ (green shaded region), indicating that an AC magnetic field in the θ -direction can induce precession in this frequency range.

“partially trapped” and “gyroscope” cases, respectively. The left plots show the behavior of the eigenvalues $\lambda_{\max}, \lambda_{\min}$ of $\chi(\omega)$. The right plots show the elements of $\chi(\omega)$. We show in green the regions where precession is possible, which occurs when the off-diagonal elements are larger than the diagonal elements.

III. MAGNETIC-FIELD SENSITIVITY

In this section, we compute the sensitivity of various ferromagnet setups to an applied AC magnetic field. First, we review the dominant noise sources present in such a setup, accounting for noise in both angular directions using the formalism developed in Sec. II. Then, we consider the physical constraints of a levitated ferromagnet setup in order to determine optimal parameters for a future levitated setup. These parameters are shown in Tab. I, along with parameters representative of an existing setup and ones for a space-based freefall setup. Finally, we review other potential noise sources.

A. Dominant noise sources

Now, we characterize the relevant noise sources in our system. The noise analysis presented in this subsection parallels the analysis in Ref. [29], but we account for the

motion of the ferromagnet in both angular directions. To this end, we generalize many of the scalar quantities introduced in Ref. [29] to 2×2 matrices [as we did for the mechanical susceptibility $\chi(\omega)$ in Eq. (31)].

We consider three primary noise sources: thermal, imprecision, and back-action noise. Let us first begin with thermal noise. The thermal torque noise acting on the ferromagnet is given by

$$S_{\tau\tau}^{\text{th}}(\omega) = \begin{pmatrix} S_{\tau\tau,\theta\theta}^{\text{th}}(\omega) & S_{\tau\tau,\theta\phi}^{\text{th}}(\omega) \\ S_{\tau\tau,\phi\theta}^{\text{th}}(\omega) & S_{\tau\tau,\phi\phi}^{\text{th}}(\omega) \end{pmatrix} \quad (33)$$

$$= 4k_B I \gamma T \begin{pmatrix} 1 & 0 \\ 0 & 1 \end{pmatrix}, \quad (34)$$

where $S_{\tau\tau,\alpha\beta}$ represents the cross-correlation between torque noise in the α - and β -directions, and γ is the dissipation rate of the system.¹¹ An applied magnetic field induces a torque

$$\tau = -\mu \hat{\mathbf{n}} \times \mathbf{B}, \quad (35)$$

where $\mu = N\hbar\gamma_e/2$ is the magnetic moment of the ferro-

¹¹ We assume that the dissipation rate is the same for both modes, e.g., in the case of damping due to gas collisions. For a more general case, one can extend this formalism directly.

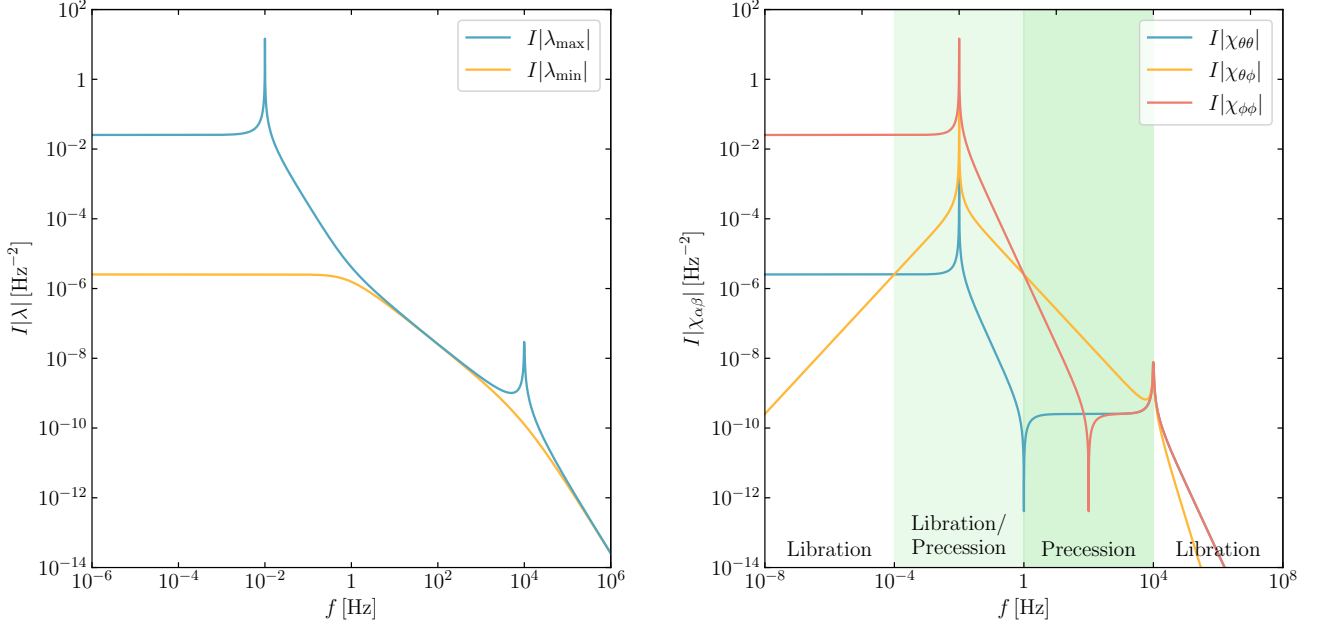


FIG. 2. Same as Fig. 1, but in the “gyroscope” case. In these plots, we set $\omega_I = 2\pi \cdot 10^4$ Hz, $v_{\theta\theta} = 2\pi \cdot 1$ Hz, $v_{\phi\phi} = 2\pi \cdot 10^{-4}$ Hz, and $j_n = 1$. Note that the resonances in the left plot are now at $\omega = \sqrt{v_{\theta\theta}v_{\phi\phi}}$ and $\omega = \omega_I$, and that the blue line exhibits the scaling behavior indicated in Eq. (32). On the right, note that $|\chi_{\theta\phi}| > |\chi_{\theta\theta}|, |\chi_{\phi\phi}|$ for $j_n\omega_I \gg \omega \gg v_{\theta\theta}/j_n$ (darker green shaded region), indicating that there is precession in both directions in this frequency range.

magnet, or equivalently

$$\begin{pmatrix} \tau_\theta \\ \tau_\phi \end{pmatrix} = \mu \begin{pmatrix} 0 & 1 \\ -1 & 0 \end{pmatrix} \begin{pmatrix} B_\theta \\ B_\phi \end{pmatrix}. \quad (36)$$

Then the torque noise in Eq. (34) can be translated into a magnetic-field noise

$$S_{BB}^{\text{th}}(\omega) = \frac{1}{\mu^2} \begin{pmatrix} 0 & -1 \\ 1 & 0 \end{pmatrix} S_{\tau\tau}^{\text{th}}(\omega) \begin{pmatrix} 0 & 1 \\ -1 & 0 \end{pmatrix} \quad (37)$$

$$= \frac{4k_B I \gamma T}{\mu^2} \begin{pmatrix} 0 & -1 \\ 1 & 0 \end{pmatrix} \begin{pmatrix} 1 & 0 \\ 0 & 1 \end{pmatrix} \begin{pmatrix} 0 & 1 \\ -1 & 0 \end{pmatrix} \quad (38)$$

$$= \frac{4k_B I \gamma T}{\mu^2} \begin{pmatrix} 1 & 0 \\ 0 & 1 \end{pmatrix}. \quad (39)$$

Imprecision and back-action are noise sources related to the readout scheme. For concreteness, here we will consider a readout scenario that utilizes two SQUIDS (to read the two angular modes of the ferromagnet). Each SQUID exhibits both a flux noise $S_{\varphi\varphi,j}$ and current noise $S_{JJ,j}$ (for $j = 1, 2$).¹² They can be combined to define the energy resolution $\kappa_j = \sqrt{S_{\varphi\varphi,j}S_{JJ,j}}$ of the SQUID, which is bounded below by the uncertainty relation $\kappa_j \geq \hbar$ [30]. Currents in the SQUIDS lead to back-action torques on

the ferromagnet. These can be defined by a coupling matrix

$$\begin{pmatrix} \tau_\theta \\ \tau_\phi \end{pmatrix} = \boldsymbol{\tau} = -\hat{\mathbf{n}} \times \eta \mathbf{J} \quad (40)$$

$$= \begin{pmatrix} 0 & 1 \\ -1 & 0 \end{pmatrix} \begin{pmatrix} \eta_{\theta 1} & \eta_{\theta 2} \\ \eta_{\phi 1} & \eta_{\phi 2} \end{pmatrix} \begin{pmatrix} J_1 \\ J_2 \end{pmatrix}. \quad (41)$$

(Note that if we wish to reduce to the case of a single-SQUID readout, this can be done by taking $\eta_{\theta 2}, \eta_{\phi 2} \rightarrow 0$.) Likewise, fluxes in the SQUIDS correspond to angular displacements $\hat{\mathbf{n}} = (\eta^{-1})^T \boldsymbol{\varphi}$. We can then express the current and flux noise as torque and angular uncertainties, respectively

$$S_{\tau\tau}^{\text{back}} = \begin{pmatrix} 0 & 1 \\ -1 & 0 \end{pmatrix} \eta S_{JJ} \eta^T \begin{pmatrix} 0 & -1 \\ 1 & 0 \end{pmatrix} \quad (42)$$

$$= \begin{pmatrix} 0 & 1 \\ -1 & 0 \end{pmatrix} \eta \begin{pmatrix} S_{JJ,1} & 0 \\ 0 & S_{JJ,2} \end{pmatrix} \eta^T \begin{pmatrix} 0 & -1 \\ 1 & 0 \end{pmatrix} \quad (43)$$

$$S_{\hat{n}\hat{n}}^{\text{imp}} = (\eta^{-1})^T S_{\varphi\varphi} \eta^{-1} \quad (44)$$

$$= (\eta^{-1})^T \begin{pmatrix} S_{\varphi\varphi,1} & 0 \\ 0 & S_{\varphi\varphi,2} \end{pmatrix} \eta^{-1}. \quad (45)$$

Much like the thermal noise, it is straightforward to translate the back-action noise into a magnetic-field noise

$$S_{BB}^{\text{back}}(\omega) = \frac{1}{\mu^2} \eta S_{JJ} \eta^T. \quad (46)$$

The imprecision noise, on the other hand, requires the use of $\chi(\omega)$, as in Eq. (30), in order to translate it into a

¹² In this work, we neglect any correlations $S_{\varphi J}$ between flux and current noise.

magnetic-field noise¹³

$$S_{BB}^{\text{imp}}(\omega) = \frac{1}{\mu^2} \chi(\omega)^{-1} (\eta^{-1})^T S_{\varphi\varphi} \eta^{-1} \chi(\omega)^{-1}. \quad (47)$$

The total magnetic-field noise will be given by

$$S_{BB}^{\text{tot}}(\omega) = S_{BB}^{\text{th}}(\omega) + S_{BB}^{\text{imp}}(\omega) + S_{BB}^{\text{back}}(\omega). \quad (48)$$

As the imprecision and back-action noise scale in opposite ways with the coupling η , there exists a trade-off between them, and so we should consider our choice of η carefully. Let us begin by making a slight change of variables to Eq. (46) and Eq. (47); that is, let us define

$$\kappa = S_{JJ}^{1/2} S_{\varphi\varphi}^{1/2} = \begin{pmatrix} \kappa_1 & 0 \\ 0 & \kappa_2 \end{pmatrix} \quad (49)$$

$$\tilde{\eta} = \eta S_{JJ}^{1/4} S_{\varphi\varphi}^{-1/4}, \quad (50)$$

so that we may write

$$S_{BB}^{\text{back}}(\omega) = \frac{1}{\mu^2} \tilde{\eta} \kappa \tilde{\eta}^T \quad (51)$$

$$S_{BB}^{\text{imp}}(\omega) = \frac{1}{\mu^2} \chi(\omega)^{-1} (\tilde{\eta}^{-1})^T \kappa \tilde{\eta}^{-1} \chi(\omega)^{-1}. \quad (52)$$

As we can see from Figs. 1 and 2, the response of the system is maximized for frequencies at/below the lowest resonance, and so this is where we will get the best sensitivity. As such, we will choose η to maximize our sensitivity in this region. Note that in this frequency range, the last term in Eq. (31) always dominates (regardless of what parameter regime we are in). Therefore, $\chi(\omega)$ is always nearly diagonal. Since κ is also diagonal, it will be advantageous for us to take $\tilde{\eta}$ diagonal as well. In that case, we find¹⁴

$$S_{BB}^{\text{back}}(\omega) = \frac{1}{\mu^2} \begin{pmatrix} \kappa_1 \tilde{\eta}_1^2 & 0 \\ 0 & \kappa_2 \tilde{\eta}_2^2 \end{pmatrix} \quad (53)$$

$$S_{BB}^{\text{imp}}(\omega) \approx \frac{1}{\mu^2} \begin{pmatrix} \kappa_1 \tilde{\eta}_1^{-2} V_{\theta\theta}^2 & 0 \\ 0 & \kappa_2 \tilde{\eta}_2^{-2} V_{\phi\phi}^2 \end{pmatrix}, \quad (54)$$

¹³ One may consider adding a damping term (corresponding to the quality factor of the system) to the definition of $\chi(\omega)$ in Eq. (31), in order to regulate the behavior of this expression near the resonances of $\chi(\omega)$. Below, we will consider parameters such that imprecision noise never dominates on-resonance, so it is reasonable to exclude this damping term.

¹⁴ In many cases, Eq. (54) is not the correct expression for S_{BB}^{imp} , as we have neglected the contributions from the off-diagonal elements of $\chi(\omega)^{-1}$. Nevertheless, Eq. (54) possesses the correct eigenvalues and eigenvectors for S_{BB}^{imp} , which are the only properties we require. This is because Eq. (54) has the correct value for $S_{BB,\theta\theta}^{\text{imp}}$, which is much larger than the other elements. This ensures that $\kappa_1 \tilde{\eta}_1^{-2} V_{\theta\theta}^2 / \mu^2$ is indeed an eigenvalue of S_{BB}^{imp} , with corresponding eigenvector approximately equal to $\hat{\theta}$. The other eigenvector is fixed by orthogonality, and the other eigenvalue is fixed by the determinant of S_{BB}^{imp} [which depends negligibly on the off-diagonal elements of $\chi(\omega)^{-1}$].

where the approximation in Eq. (54) holds for $\omega \leq \sqrt{\omega_I v_{\phi\phi}}, \sqrt{v_{\theta\theta} v_{\phi\phi}}$, and we have defined $V_{\alpha\beta} = \partial_\alpha \partial_\beta V|_{(\theta_0, \phi_0)}$ and set

$$\tilde{\eta} = \begin{pmatrix} \tilde{\eta}_\theta & 0 \\ 0 & \tilde{\eta}_\phi \end{pmatrix}. \quad (55)$$

Once we have chosen $\tilde{\eta}$ to be diagonal, we see that the choice of coupling along each axis is independent. As shown in Appendix A, the total sensitivity of our system ultimately depends on the sensitivity in both directions, but it will be predominantly determined by the sensitivity along the more sensitive axis. Let us first address how to choose the coupling for a single axis. There are two cases one should consider. Firstly, if the thermal noise is larger than the geometric mean of the back-action and low-frequency imprecision noise, that is,

$$S_{BB,\alpha\alpha}^{\text{th}} \geq \sqrt{S_{BB,\alpha\alpha}^{\text{imp}}(\omega = 0) \cdot S_{BB,\alpha\alpha}^{\text{back}}}, \quad (56)$$

or equivalently

$$\tilde{\eta}_\alpha^{(\text{res})} \geq \tilde{\eta}_\alpha^{(\text{broad})}, \quad (57)$$

where

$$\tilde{\eta}_\alpha^{(\text{res})} = \sqrt{\frac{4k_B I \gamma T}{\kappa_j}} \quad (58)$$

$$\tilde{\eta}_\alpha^{(\text{broad})} = \sqrt{V_{\alpha\alpha}}, \quad (59)$$

then both imprecision and back-action noise can be made subdominant to thermal noise at frequencies at/below the resonance of this mode. This is achieved so long as

$$\tilde{\eta}_\alpha^{(\text{res})} \geq \tilde{\eta}_\alpha \geq [\tilde{\eta}_\alpha^{(\text{broad})}]^2 / \tilde{\eta}_\alpha^{(\text{res})}. \quad (60)$$

The closer $\tilde{\eta}$ is to the upper bound in Eq. (60), the better the sensitivity will be at higher frequencies (as imprecision noise always dominates at sufficiently high frequencies), but if the primary goal is to maximize sensitivity at/below the resonance, then any coupling in this range will suffice.

If Eq. (57) is not met, then one of imprecision or back-action noise will always dominate at low frequencies. There are then two possible approaches. If we wish to maximize the sensitivity on-resonance, then we should set the back-action noise equal to thermal noise, i.e. the choice of $\tilde{\eta}$ in Eq. (58). If, instead, we wish to optimize for sensitivity at low frequencies, then we should set back-action noise equal to low-frequency imprecision noise, i.e., the choice of $\tilde{\eta}$ in Eq. (59). In this way, an individual mode can be optimized for either resonant or broadband detection. If two SQUIDs are utilized to track both modes, then we can make this choice for each mode separately.

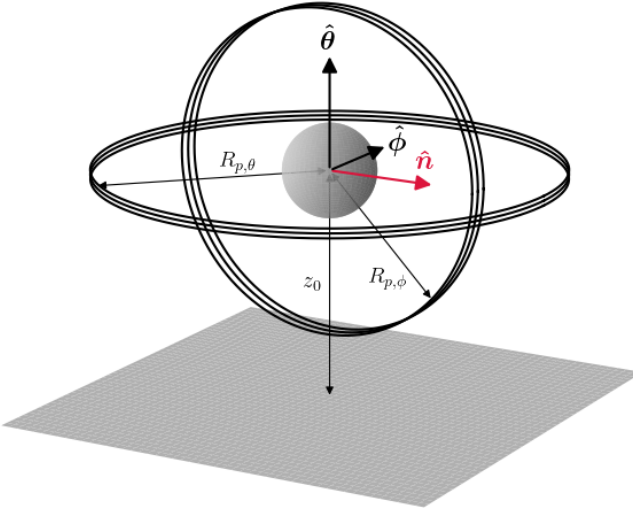


FIG. 3. Scheme of the circular pick-up coils considered for the estimation of coupling. The spherical magnet at equilibrium height z_0 has its magnetic dipole oriented along \hat{n} . Rotations along the spherical angles θ and ϕ are detected with maximum efficiency by the horizontal coil (radius $R_{p,\theta}$) and vertical coil (radius $R_{p,\phi}$) respectively.

B. Parameter estimation

In this section, we estimate the parameters that can be realistically achieved in a future levitation setup. In particular, we need estimations for the ferromagnet parameters, the trapping potential V , the temperature T and dissipation rate γ that determine the thermal noise, and finally, the energy resolution κ and coupling $\tilde{\eta}$ of the readout.

For concreteness, we consider a setup with a permanent hard ferromagnetic sphere with magnetization $M = B_s/\mu_0$ (with B_s saturation remanence field), density ρ , and radius R , levitated via the Meissner effect above a type-I superconducting plane [3, 4], i.e. with a potential of the form in Eq. (4). We consider the plane to be made of lead, which has a critical field $B_c = 80$ mT. The equilibrium levitation height can be expressed as [3]

$$z_0 = \left(\frac{\mu_0 M^2 R^3}{16 \rho g} \right)^{\frac{1}{4}}. \quad (61)$$

A typical neodymium-based rare earth alloy used in current experiments features $M \approx 7 \times 10^5$ A/m and $\rho \approx 7400$ kg/m³. For these parameters, the maximum field produced by the magnet at the superconducting surface

$$B_{\text{surf}} = \frac{2B_s}{3} \left(\frac{R}{z_0} \right)^3 \quad (62)$$

increases with R and approaches the critical field for $R \approx 35$ mm. This is an ultimate upper limit on R for pure Meissner levitation above lead. A safe choice for a

future experiment is $R = 2$ mm, which implies a field at the surface of ~ 9 mT, one order of magnitude below the critical field. Levitating a larger magnet would require using a type-II superconductor [31], in which case modeling would be more complex, and additional dissipation from vortex motion would arise.

The magnetic confinement in the polar direction $V_{\theta\theta}$ can be determined via Eq. (4). The azimuthal confinement $V_{\phi\phi}$ has been recently shown to be tunable in a wide range between 10^{-5} and 10^{-1} times $V_{\theta\theta}$ by applying a bias field [5]. For concreteness we set $V_{\phi\phi} = 10^{-3}V_{\theta\theta}$. For the thermal noise we set $\gamma = 2 \times 10^{-6}$ Hz and $T = 50$ mK. Such values appear within reach and have been approached by a recent experiment [32], where $\gamma \lesssim 10^{-5}$ Hz was measured at the operating temperature $T = 30$ mK. In that experiment, an excess noise of a factor 100 larger than the thermal noise was attributed to insufficient vibrational isolation. We also remark that even lower dissipation $\gamma \approx 4 \times 10^{-7}$ Hz has been measured with a nanoparticle in ultrahigh vacuum levitated within a Paul trap [33].

For the readout, we consider two circular superconducting pick-up coils. In accordance with the choice of setting $\tilde{\eta}$ to be diagonal [see Eq. (55)], we optimally orient the coils to sense rotations along the θ - and ϕ -directions, with number of loops $N_{p,\alpha}$ and radius $R_{p,\alpha}$. This arrangement is sketched in Fig. 3. Each pick-up coil, with inductance L_p , is connected to the input coil of a DC SQUID. The latter has inductance L_S , the input coil has inductance L_i , and they have mutual inductance $M_i = k\sqrt{L_i L_S}$, with $k \leq 1$ a geometrical coupling factor.

A DC SQUID can be modeled as a linear detector of magnetic flux, with imprecision flux noise $S_{\varphi_S \varphi_S}$ and circulating current back-action noise $S_{J_S J_S}$. These can alternatively be expressed as flux/current energy resolution $\kappa_\varphi = S_{\varphi_S \varphi_S}/L_S$ and $\kappa_J = S_{J_S J_S} L_S$ (so that $\kappa^2 = \kappa_\varphi \kappa_J$).¹⁵ The advantage of this normalization is that the quantum limit for each noise source is given by $\kappa_\varphi, \kappa_J \geq \hbar$.

In a pick-up coil configuration, the flux effectively coupled into the SQUID is $\varphi_S = (M_i/L)\varphi$, where $\varphi = \eta_\theta \theta$ or $\varphi = \eta_\phi \phi$ is the flux coupled into the pick-up coil by a rotation angle θ or ϕ of the ferromagnet. Here, $L = L_i + L_p$ is the total inductance of the superconducting flux transformer loop. Likewise, a circulating current in the SQUID J_S translates into a current $J = (M_i/L)J_S$ in the pick-up coil. This is shown in Fig. 4. The flux transformer loop thus behaves as an equivalent SQUID with inductance L , imprecision noise $S_{\varphi\varphi} = S_{\varphi_S \varphi_S}/(M_i/L)^2$ and back-action noise $S_{JJ} = S_{J_S J_S}(M_i/L)^2$. The energy product $\kappa = S_{JJ} S_{\varphi\varphi}$ is invariant, while $\tilde{\eta} = (M_i/L)\tilde{\eta}_S$ is rescaled.

¹⁵ We note that in the literature, these energy resolutions are sometimes defined as $\epsilon_\varphi = \kappa_\varphi/2$ and $\epsilon_J = \kappa_J/2$. Here, we omit the factor of two to agree with our definition of κ .

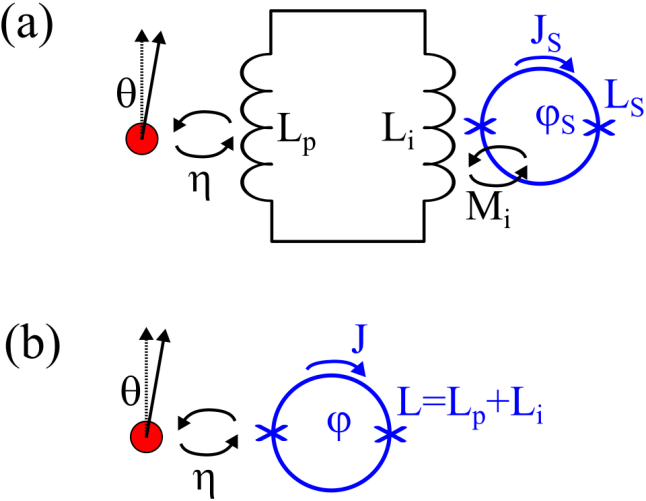


FIG. 4. A SQUID connected through a superconducting pick-up coil to the ferromagnet motion is equivalent to a SQUID directly connected to the ferromagnet, with the backward scaling $J/J_S = M_i/L$ and the forward scaling $\varphi_S/\varphi = M_i/L$. Here, M_i is the mutual inductance between the input coil and SQUID, and $L = L_i + L_p$. The effective coupling η to the equivalent SQUID coincides with the coupling to the pick-up coil. The imprecision and back-action noises $S_{\phi\phi}$ and S_{JJ} of the equivalent SQUID are rescaled by $(M_i/L)^{-2}$ and $(M_i/L)^2$ with respect to the real SQUID noises. As a result, κ is the same for the effective and real SQUIDs, while $\tilde{\eta}$ is rescaled by M_i/L .

The coupling η between the rotating ferromagnet and pick-up coil for the optimal geometrical configuration shown in Fig. 3 is given by

$$\eta = \frac{N_p \mu_0 \mu}{2R_p}. \quad (63)$$

If one wishes to increase the coupling $\tilde{\eta}$, one should maximize the product $\eta \cdot M_i/L$. This is most easily done by modifying the pick-up coil, specifically by varying the number of loops. A pick-up coil made of N_p circular superconducting loops of radius R with wire radius a has inductance

$$L_p = N_p^2 \mu_0 R_p \left[\log \left(\frac{8R_p}{a_p} \right) - 2 \right]. \quad (64)$$

As a function of N_p , the product $\eta \cdot M_i/L$ will be maximized when $L_p = L_i$. (Alternatively, if one wishes to reduce $\tilde{\eta}$, the number of coils can be decreased/increased.)

In Tab. I, we show sample parameters for three different setups: ones representative of an existing levitated setup [5], ones for a future levitated setup, and ones for a space-based freefall setup. Their corresponding magnetic field sensitivities $S_{BB}(f)$ are shown in Fig. 5. The future setup takes the ferromagnet (R , M , and ρ) and system parameters (T , γ , and $V_{\phi\phi}$) described above. For the readout, we take $R_p = 8$ mm, $a_p = 100$ μ m, $L_S = 80$ pH, $L_i = 1.8$ μ H, and $k = 0.85$. With these

values, the optimal number of loops (to achieve $L_p \approx L_i$) is $N_p = 6$. We also assume a quantum-limited readout $\kappa = \kappa_\varphi = \kappa_J = \hbar$. With these parameter choices, we see that the system exhibits the “trapped” behavior described in Sec. II C because $v_{\theta\theta}, v_{\phi\phi} \gg \omega_I$. (We set $j_n = 1$ in all cases.) Moreover, both modes satisfy Eq. (60), so the readout is appropriately coupled.

The existing case uses ferromagnet and system parameters comparable to the setup in Ref. [5]. For the readout of the θ -mode, we take the same parameters as in the future setup, but with a smaller pick-up loop $R_p = 1$ mm and worse energy resolution $\kappa = \kappa_\varphi = \kappa_J = 1000\hbar$. With this pick-up loop radius, the optimal number of coils is $N_p = 25$. For the readout of the ϕ -mode, the setup in Fig. 3 is not achievable since the equilibrium point of the ferromagnet is so close to the superconducting plane $z_0 \approx 250$ μ m. Instead, different geometries may be realized. For instance, in Ref. [5], the ϕ -mode is read out using a figure-eight-shaped coil lying in a plane above the ferromagnet. Such a geometry will naturally exhibit a weaker coupling than the θ -readout. In Tab. I, we simply fix a coupling $\tilde{\eta}_\phi = 5 \times 10^{-9} \sqrt{J}$ comparable to that of Ref. [5], without focusing on any particular geometric realization. In this case, neither mode satisfies Eq. (60), so both modes are undercoupled.

Finally, the freefall case considers a space-based experiment with parameters comparable to the LISA Pathfinder mission [34, 35]. We take a ferromagnet of similar dimensions to the LISA test mass (but we take a neodymium sphere rather than a gold cube). We consider the system to be at room temperature $T = 300$ K with a dissipation rate $\gamma = 10^{-10}$ Hz that produces a thermal noise slightly better than LISA Pathfinder’s angular sensitivity [34]. The ferromagnet will experience some weak trapping from stray magnetic fields inside the apparatus. The Sun’s magnetic field near LISA’s position averages ~ 5 nT, which can be reduced by a few orders of magnitude with moderate magnetic shielding. On the other hand, the shielding itself will exhibit some residual magnetization, which will likely dominate the stray fields inside the apparatus. We assume a residual magnetic field of ~ 300 pT [36],¹⁶ resulting in a trapping potential $V \sim 7 \times 10^{-9}$ J. Finally, a SQUID readout will be difficult to implement effectively at room temperature. Instead, LISA utilizes an interferometric readout with positional imprecision noise $\sqrt{S_{xx}} \sim 3 \times 10^{-14}$ m/ $\sqrt{\text{Hz}}$ [35], which translates to an angular imprecision $\sqrt{S_{\hat{n}\hat{n}}} \sim 10^{-12}$ rad/ $\sqrt{\text{Hz}}$. Assuming a quantum-limited readout $\kappa = \hbar$, this corresponds to a coupling $\tilde{\eta} \sim 10^{-5}$ J. We see that both modes satisfy

¹⁶ We note that it may be possible to reduce the stray fields in the apparatus further [37, 38]. Ultimately, trapping by stray fields does not limit our final sensitivity. This will only affect the imprecision noise at low frequencies, but as can be seen from the bottom plot of Fig. 5, we are dominated by thermal noise at low frequencies.

| Parameter | Existing | Future | Freefall |
|---|---|--|--|
| Ferromagnet radius R | $20\text{ }\mu\text{m}$ | 2 mm | 2 cm |
| Ferromagnet magnetization M | | $7 \times 10^5 \text{ A/m}$ | |
| Ferromagnet density ρ | | 7400 kg/m^3 | |
| Temperature T | 4 K | 50 mK | 300 K |
| Dissipation rate γ | 10^{-2} Hz | $2 \times 10^{-6} \text{ Hz}$ | 10^{-10} Hz |
| Azimuthal trapping $V_{\phi\phi}$ | 10^{-14} J | $10^{-3} V_{\theta\theta}$ | $7 \times 10^{-9} \text{ J}$ |
| Energy resolution $\kappa_\theta = \kappa_\phi$ | $1000\hbar$ | \hbar | \hbar |
| Polar coupling $\tilde{\eta}_\theta$ | $1.1 \times 10^{-7} \sqrt{\text{J}}$ | $3.7 \times 10^{-3} \sqrt{\text{J}}$ | $10^{-5} \sqrt{\text{J}}$ |
| Azimuthal coupling $\tilde{\eta}_\phi$ | $5 \times 10^{-9} \sqrt{\text{J}}$ | $3.7 \times 10^{-3} \sqrt{\text{J}}$ | $10^{-5} \sqrt{\text{J}}$ |
| $\tilde{\eta}_\theta^{(\text{res})} = \tilde{\eta}_\phi^{(\text{res})}$ | $9.1 \times 10^{-7} \sqrt{\text{J}}$ | $4.6 \times 10^{-3} \sqrt{\text{J}}$ | $2.5 \sqrt{\text{J}}$ |
| $\tilde{\eta}_\theta^{(\text{broad})}$ | $6.4 \times 10^{-7} \sqrt{\text{J}}$ | $3.6 \times 10^{-3} \sqrt{\text{J}}$ | $10^{-5} \sqrt{\text{J}}$ |
| $\tilde{\eta}_\phi^{(\text{broad})}$ | $10^{-7} \sqrt{\text{J}}$ | $1.1 \times 10^{-4} \sqrt{\text{J}}$ | $10^{-5} \sqrt{\text{J}}$ |
| ω_I | $2\pi \cdot 0.53 \text{ Hz}$ | $2\pi \cdot 5.3 \times 10^{-5} \text{ Hz}$ | $2\pi \cdot 5.3 \times 10^{-7} \text{ Hz}$ |
| $v_{\theta\theta}$ | $2\pi \cdot 4.9 \times 10^5 \text{ Hz}$ | $2\pi \cdot 1.6 \times 10^7 \text{ Hz}$ | $2\pi \cdot 0.12 \text{ Hz}$ |
| $v_{\phi\phi}$ | $2\pi \cdot 1.2 \times 10^4 \text{ Hz}$ | $2\pi \cdot 1.6 \times 10^4 \text{ Hz}$ | $2\pi \cdot 0.12 \text{ Hz}$ |

TABLE I. Parameters choices for various setups. Here, we show three sets of parameters: one representative of an existing levitated setup [5] (but with an additional readout mode; see text), a future levitated setup, and a space-based freefall setup with parameters comparable to LISA Pathfinder. Each section of the table includes ferromagnet parameters, system parameters, readout parameters, and resulting quantities defined in Secs. II and III A. In the first two cases, the polar trapping $V_{\theta\theta}$ can be computed via Eq. (4), while in the third case, it is the same as $V_{\phi\phi}$. In the future setup, both modes satisfy Eq. (60), so the readout is appropriately coupled. In the existing setup, both modes are undercoupled. In the freefall setup, they satisfy Eq. (60), but the sensitivity would benefit at higher frequencies from an even larger coupling. In all three cases, the system exhibits “trapped” behavior (i.e. $v_{\theta\theta}, v_{\phi\phi} \gg \omega_I$).

Eq. (60), so that the low-frequency sensitivity is dominated by thermal noise. However, since $\tilde{\eta}$ is far from the upper bound of Eq. (60), the high-frequency sensitivity could be improved if the coupling can be increased further. Also note that despite the fact that the experiment is in freefall, this case still exhibits the “trapped” rather than “gyroscope” behavior (i.e., $v_{\theta\theta}, v_{\phi\phi} \gg \omega_I$ still). To achieve the gyroscope behavior with such a large ferromagnet would require significantly better shielding.

C. Other noise sources

Before we move on to estimate the sensitivity of these setups to DM, we note a couple of additional sources of noise, which are not inherent but may take additional care to mitigate. The first is vibrational noise, which can lead to translational motion of the ferromagnet if not properly attenuated. If the translational and rotational motions of the ferromagnet exhibit some small coupling (see footnote 7), this will translate into noise in its angular orientation $\hat{\mathbf{n}}$ (similar to imprecision noise). The angular imprecision noise for the future levitated setup is $\sqrt{S_{\hat{\mathbf{n}}\hat{\mathbf{n}}}} \sim 3 \times 10^{-15} \text{ rad}/\sqrt{\text{Hz}}$. Assuming a $\mathcal{O}(0.01)$ coupling between the translational and rotational modes, this setup would require a vibrational noise $\sqrt{S_{\mathbf{xx}}} \lesssim 6 \times 10^{-16} \text{ m}/\sqrt{\text{Hz}}$ in order for vibrations to be subdominant. The corresponding requirement for the existing and freefall setups is $\sqrt{S_{\mathbf{xx}}} \lesssim 10^{-12} \text{ m}/\sqrt{\text{Hz}}$. LIGO

has achieved vibrational noises below these thresholds for frequencies $f \gtrsim 10 \text{ Hz}$ [39].

Another noise source of concern is $1/f$ noise in the SQUID readout, which typically dominates at low frequencies $f \lesssim 10 \text{ kHz}$ and results in flux noise $\sqrt{S_{\varphi\varphi}} \sim 5 - 10 \mu\Phi_0/\sqrt{\text{Hz}}$ at $f \sim 1 \text{ Hz}$ [40] (compared to the much lower noise $\sqrt{S_{\varphi\varphi}} \sim 0.04 \mu\Phi_0/\sqrt{\text{Hz}}$ assumed in our future setup). Methods to substantially reduce $1/f$ noise by material engineering have demonstrated suppression down to $\sqrt{S_{\varphi\varphi}} \sim 0.3 \mu\Phi_0/\sqrt{\text{Hz}}$ at $f \sim 1 \text{ Hz}$ [40]. A more complex approach is to mitigate $1/f$ noise by up-converting the signal to a higher pump frequency where $1/f$ noise is negligible. This can be achieved via a capacitor bridge transducer [41, 42], or an inductance bridge transducer [43]. Henceforth, we assume that our readout implements such a scheme. This allows us to neglect $1/f$ noise and validates our assumption of frequency-independent flux noise.

IV. SEARCHING FOR ULTRALIGHT DM

In this section, we introduce a few ultralight DM candidates/couplings which could be detected with ferromagnets. All of these candidates manifest in laboratory experiments as effective/physical AC magnetic fields, and so a ferromagnet will respond to these DM candidates in the manner described in Sec. II. We can then use the magnetic-field sensitivities computed in Sec. III to

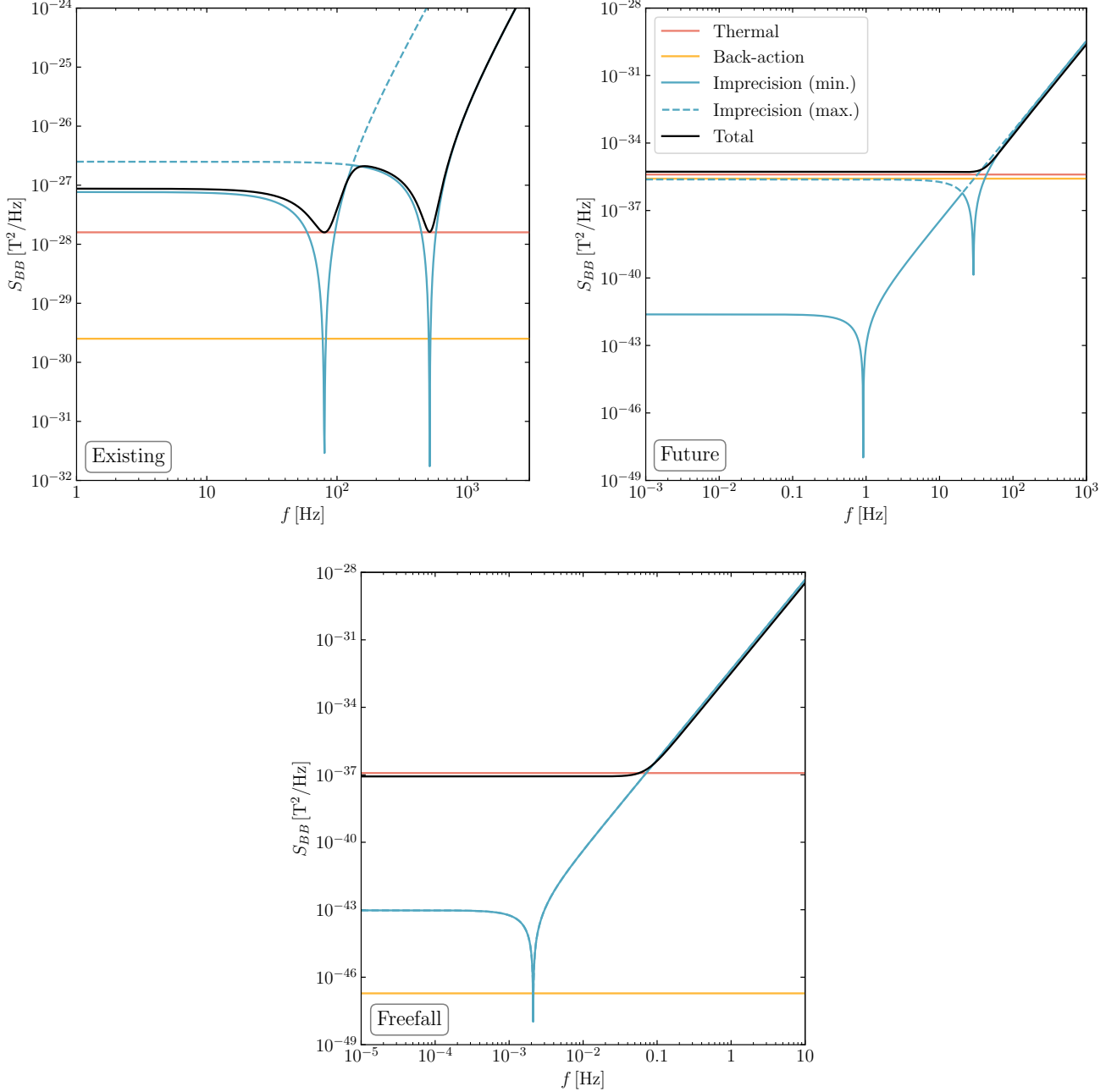


FIG. 5. Magnetic field sensitivities for the three setups shown in Tab. I. We show the total noise in black, the thermal contribution in red, the backaction contribution in yellow, and the imprecision contribution in blue. (For the imprecision noise, the smaller eigenvalue of S_{BB}^{imp} , which dominates the sensitivity, is shown as solid, while the larger eigenvalue is dashed.) Note that the future and freefall setups have broadband sensitivity because they are adequately coupled [satisfy Eq. (60)], while the existing case has resonant sensitivity (in both modes) because it is undercoupled. The freefall setup demonstrates better sensitivity than the future setup at low frequencies, but becomes dominated by imprecision noise at much lower frequencies than in the future case. This can be improved by increasing the coupling towards the upper bound in Eq. (60). Both cases show significantly better sensitivity than the existing case.

project the sensitivity of ferromagnets to these DM candidates. In this section, we consider two possible interactions of axion DM: a coupling to electrons g_{ae} and a coupling to photons $g_{a\gamma}$. The former directly causes

precession of electron spins, while the latter creates an observable magnetic field (which in turn leads to precession of magnetic moments). In addition, we also consider DPDM with kinetic mixing ε , which generates a similar

observable magnetic field.

A. Axion-electron coupling

An axionlike particle a , with mass m_a , is a pseudoscalar which may generically exhibit various interactions with SM particles. One such possible interaction is a coupling to electrons via the operator

$$\mathcal{L}_{ae} \supset \frac{g_{ae}\sqrt{\hbar^3 c}}{2m_e} \partial_\mu a \bar{\psi}_e \gamma^\mu \gamma_5 \psi_e, \quad (65)$$

where m_e is the electron mass and ψ_e is its wavefunction. When the electron is non-relativistic, this leads to a coupling between the axion gradient and electron spins, i.e. a Hamiltonian of the form

$$H \supset \frac{g_{ae}\sqrt{\hbar^3 c}}{2m_e} \boldsymbol{\sigma}_e \cdot \nabla a \equiv -\gamma_e \boldsymbol{S}_e \cdot \boldsymbol{B}_{ae}, \quad (66)$$

where $\boldsymbol{S}_e = \frac{\hbar}{2} \boldsymbol{\sigma}_e$ is the spin of the electron (and $-\gamma_e \boldsymbol{S}_e$ is its magnetic moment). We then see that an axion gradient (or “axion wind”) has the same effect on an electron spin as an effective magnetic field

$$\boldsymbol{B}_{ae} = -\frac{2g_{ae}\sqrt{\hbar c}}{g_e e} \nabla a. \quad (67)$$

As a ferromagnet is composed of many polarized electrons spins, the axion wind will also generate a torque on the ferromagnet, just as a real magnetic field would.

If axionlike particles make up the DM, then they will also be non-relativistic. This implies that a oscillates at its Compton frequency $f_a = m_a c^2 / 2\pi\hbar$, namely

$$a(\mathbf{x}, t) \approx a_0(\mathbf{x}) \cos(2\pi f_a t). \quad (68)$$

Moreover, the spatial gradients of a are suppressed by its velocity $v_{\text{DM}} \sim 10^{-3}c$, so that

$$\nabla a \sim \frac{\mathbf{v}_{\text{DM}}}{c^2} \sqrt{2\rho_{\text{DM}}} \sin(2\pi f_a t), \quad (69)$$

where $\rho_{\text{DM}} \approx 0.3 \text{ GeV/cm}^3$ is the local DM energy density [44]. The effective magnetic field in Eq. (67) is then an AC field with frequency f_a and amplitude

$$B_{ae} \sim g_{ae} \cdot 4 \times 10^{-8} \text{ T}. \quad (70)$$

Note that the monochromatic time dependence in Eq. (68) only applies on timescales shorter than the coherence time $t_{\text{coh}} \sim c^2 / f_a v_{\text{DM}}^2$. On longer timescales, the amplitude a_0 will vary stochastically [45–49]. Equivalently, in frequency space, the AC signal will be peaked at f_a , but exhibit a linewidth $\sim 10^{-6} f_a$.

In the top left plot of Fig. 6, we show the projected sensitivity of the setups described in Tab. I to an axion-electron coupling for $t_{\text{int}} = 1 \text{ yr}$ of integration time. As

shown in Appendix A, the signal-to-noise (SNR) for a given setup is

$$\text{SNR} = \frac{B_{ae}^2}{6} \sqrt{\text{Tr} \left[(S_{BB}^{\text{tot}})^{-2} \right] \cdot t_{\text{int}} \cdot \min(t_{\text{int}}, t_{\text{coh}})}, \quad (71)$$

where B_{ae} is the amplitude in Eq. (70), and the last factor accounts for the incoherence of the signal when $t_{\text{int}} > t_{\text{coh}}$. In all our projections, we set $\text{SNR} = 3$. In Fig. 6, we show a number of existing constraints on g_{ae} , including: limits based on old comagnetometer data [21]; constraints on axion-mediated forces from a torsion pendulum experiment [50]; limits on solar axions from XENONnT electronic recoil data [51]; and constraints based on the brightness of the tip of the red-giant branch [52]. Laboratory-based constraints (comagnetometers, torsion pendulum, and XENONnT) are shown in darker shades of grey, while astrophysical ones (tip of the red-giant branch) are shown in lighter shades. Fig. 6 shows that even an existing levitated ferromagnet setup can be competitive with the limits from comagnetometer or torsion pendulum experiments, while a future levitated or freefall setup can surpass all existing probes of an axion-electron coupling for $m_a \lesssim 10^{-15} \text{ eV}$.

B. Dark-photon kinetic mixing

A kinetically mixed dark photon A'_μ , with mass $m_{A'}$, is a vector boson which may mix with the SM photon. There are multiple equivalent descriptions of the interaction between the dark photon and SM photon (see Appendix A of Ref. [53] for further discussion), but the most useful for very low dark-photon masses is via the operator

$$\mathcal{L}_{A'} \supset \frac{\varepsilon}{\mu_0} \left(\frac{m_{A'} c}{\hbar} \right)^2 A_\mu A'^\mu. \quad (72)$$

We see that if A'_μ is treated as a background field, then it has an effect equivalent to a current

$$J_{\text{eff}}^\mu = -\frac{\varepsilon}{\mu_0} \left(\frac{m_{A'} c}{\hbar} \right)^2 A'^\mu. \quad (73)$$

Much like the case of axion DM, if dark photons make up the DM, they will be non-relativistic, and so should have negligible spatial gradients and oscillate at their Compton frequency $f_{A'}$. Moreover, because its equations of motion necessitate $\partial_\mu A'^\mu = 0$, then the DPDPM should have $A'^0 = 0$ (i.e., no effective charge). In this case,

$$A'(\mathbf{x}, t) \approx \text{Re} \left[\sum_{i=x,y,z} A'_{i,0} e^{-2\pi i f_{A'} t} \right], \quad (74)$$

where $A'_{i,0}$ are complex amplitudes for each spatial component of \mathbf{A}'_0 (which may have independent phases, so that \mathbf{A}' can be elliptically polarized; see footnote 9.).

The (spatial components of the) effective current \mathbf{J}_{eff} will also be approximately constant throughout space

and oscillate at frequency $f_{A'}$. This effective current will generate observable electromagnetic fields through the Ampère-Maxwell law

$$\nabla \times \mathbf{B} - \frac{\partial_t \mathbf{E}}{c^2} = \mu_0 \mathbf{J}_{\text{eff}}. \quad (75)$$

The electric field term in Eq. (75) can be ignored in contexts where the Compton wavelength $\lambda_{A'} = c/f_{A'}$ of the dark photon is much larger than the size of the experimental apparatus L .¹⁷ This implies that the primary observable effect of the dark photon is an oscillating magnetic field. Generically, this magnetic field will have amplitude

$$B_{A'} \sim \mu_0 J_{\text{eff}} L \sim \frac{\sqrt{2\mu_0 \rho_{\text{DM}} c}}{\hbar} \varepsilon m_{A'} L \quad (76)$$

$$\sim 7 \times 10^{-21} \text{ T} \left(\frac{\varepsilon}{10^{-8}} \right) \left(\frac{f_{A'}}{30 \text{ Hz}} \right) \left(\frac{L}{10 \text{ cm}} \right). \quad (77)$$

Note that by symmetry, $\mathbf{B}_{A'}$ generically vanishes at the center of the apparatus [29], and so the ferromagnet should be located off-center within the apparatus in order to experience a nonzero DPDM-induced magnetic field. In scenarios where the ferromagnet is levitated above a superconductor, this will typically be satisfied, as the ferromagnet will be much closer to the floor than the ceiling of the apparatus.

In the top right plot of Fig. 6, we show the projected sensitivity of ferromagnets to DPDM. The existing DPDM constraints shown include limits from: global unshielded magnetometer data maintained by the SuperMAG collaboration [53, 55]; unshielded magnetometer measurements made by the SNIPE Hunt collaboration [56]; magnetometer measurements taken inside a shielded room by the AMAILS collaboration [57]; non-observation of CMB-photon conversion into (non-DM) dark photons by the FIRAS instrument [58]; heating of the dwarf galaxy Leo T [59]; and resonant conversion of DPDM during the dark ages [60]. A future levitated setup could become the leading probe of DPDM across the entire mass range shown in Fig. 6. Additionally, a freefall setup could be competitive with even the leading astrophysical constraint (Leo T) at low masses $m_{A'} \lesssim 10^{-16} \text{ eV}$.

C. Axion-photon coupling

In addition to the coupling to electrons described by Eq. (65), an axionlike particle may also exhibit a coupling to photons via the operator

$$\mathcal{L} \supset \frac{g_{a\gamma} \sqrt{\hbar c^3}}{4\mu_0} a F_{\mu\nu} \tilde{F}^{\mu\nu}, \quad (78)$$

¹⁷ More specifically, by “apparatus” here, we mean the size of the conducting shield which sets the electric field boundary conditions; see Refs. [29, 53, 54] for further discussion.

where $\tilde{F}^{\mu\nu} = \frac{1}{2} \epsilon^{\mu\nu\rho\sigma} F_{\rho\sigma}$. Similar to the DPDM case, this operator is equivalent to an effective current

$$J_{\text{eff}}^\mu = -\frac{g_{a\gamma} \sqrt{\hbar c^3}}{\mu_0} \partial_\nu a \tilde{F}^{\mu\nu}. \quad (79)$$

Again taking the axion DM ansatz in Eq. (68) [with negligible spatial gradients], we find $J_{\text{eff}}^0 = 0$ and spatial components

$$\mathbf{J}_{\text{eff}} = \sqrt{\frac{c^5}{\hbar}} \frac{g_{a\gamma} m_a a_0}{\mu_0} \mathbf{B}_0 \sin(2\pi f_a t) \quad (80)$$

One crucial difference from the DPDM case is that the effective current in Eq. (80) requires the presence of a background magnetic field \mathbf{B}_0 . In our case, the magnetic field of the ferromagnet itself can act as \mathbf{B}_0 ! (See also Ref. [61] for another example where the magnetic field from a ferromagnet is used to induce axion-photon conversion.)

Unlike the DPDM case, the current in Eq. (80) will not be uniform, and so computing the resulting AC magnetic field $\mathbf{B}_{a\gamma}$ is more complicated. Generically, this must be evaluated numerically, but in Appendix B, we parametrically estimate it as

$$B_{a\gamma} \sim \mathcal{O}(0.1) \cdot \sqrt{2\hbar c \rho_{\text{DM}}} \mu_0 \frac{g_{a\gamma} \mu}{L^2} \quad (81)$$

$$\sim 3 \times 10^{-21} \text{ T} \left(\frac{g_{a\gamma}}{10^{-9} \text{ GeV}^{-1}} \right) \left(\frac{\mu}{20 \text{ mA} \cdot \text{m}^2} \right) \left(\frac{10 \text{ cm}}{L} \right)^2, \quad (82)$$

where μ is the magnetic moment of the ferromagnet, and L is again the size of the experimental apparatus.

In the bottom plot in Fig. 6, we show the projected sensitivity of ferromagnets to an axion-electron coupling. The existing constraints on $g_{a\gamma}$ shown include limits from: SuperMAG [62]; SNIPE Hunt; the CAST helioscope search for solar axions [63]; non-observation of gamma rays in coincidence with SN1987A [64]; and X-ray observations of the quasar H1821+643 from the Chandra telescope [65]. Note that in the case of an axion-photon coupling, a freefall setup may have significantly better sensitivity than a levitated setup. This is because the background magnetic field \mathbf{B}_0 is sourced by the ferromagnet itself. A ferromagnet in freefall can be much larger (and so source \mathbf{B}_0 over a larger volume) than a ferromagnet levitated over a superconductor because, in the latter case, the size is constrained by the critical field of the superconductor [see Eq. (62)]. In fact, a freefall setup can even be more sensitive than all existing constraints at low masses $m_a \lesssim 10^{-15} \text{ eV}$.

We note that in levitated setups, it may be possible to apply an additional magnetic field to act as \mathbf{B}_0 in order to enhance the sensitivity to an axion-photon coupling [although this will affect the trapping potential $V(\mathbf{x}, \hat{\mathbf{n}})$]. We leave further exploration of this idea to future work.

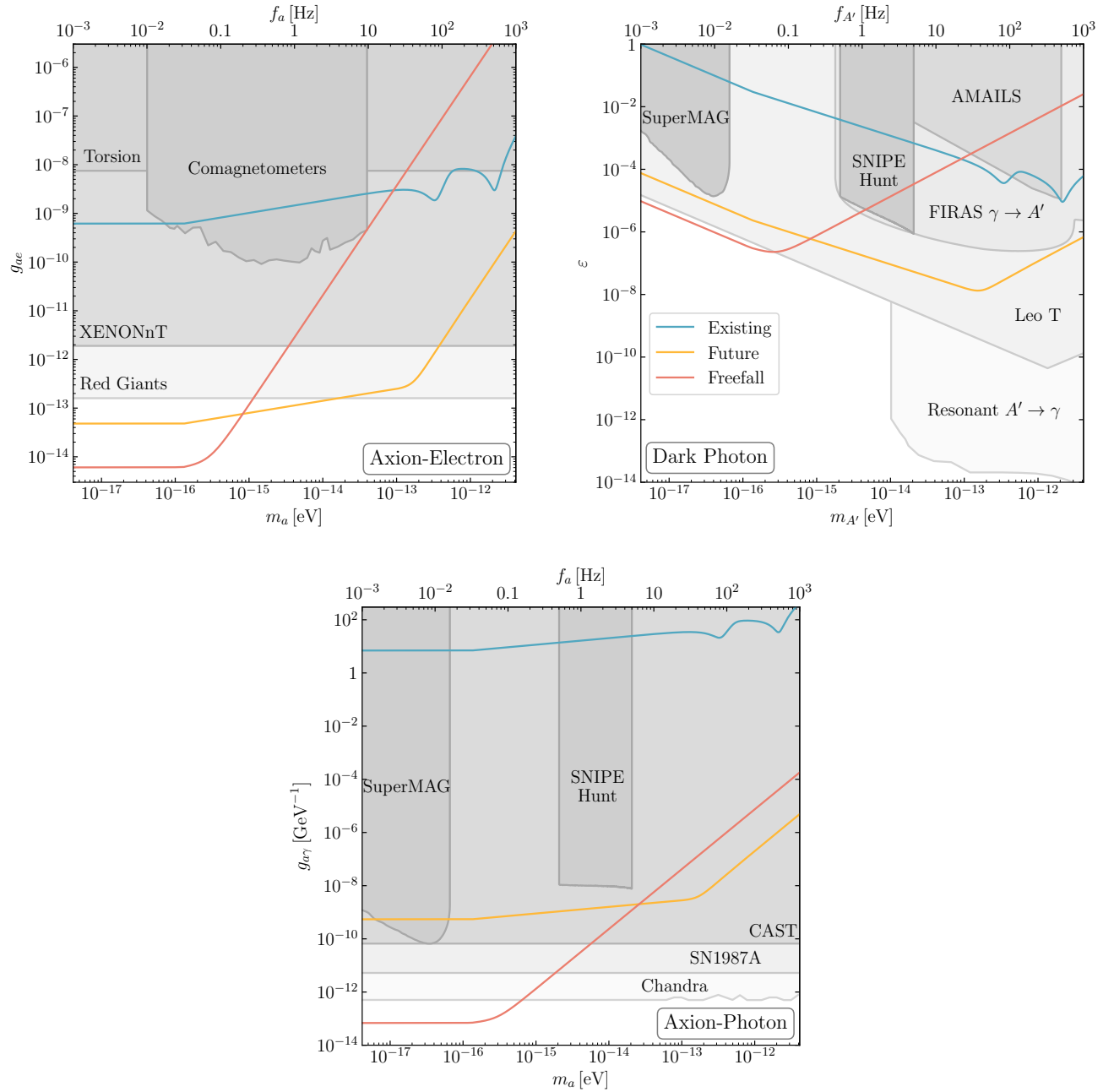


FIG. 6. Projected sensitivities of ferromagnets to an axion-electron coupling g_{ae} , DPDM kinetic mixing ϵ , and an axion-photon coupling $g_{a\gamma}$. In each case, we show three projections corresponding to the parameter choices in Tab. I. In all cases, we take an integration time of $t_{\text{int}} = 1$ yr and set $\text{SNR} = 3$. In the DPDM and axion-photon cases, we take an apparatus size of $L = 10$ cm. In darker shades of grey, we show existing laboratory constraints for these various models, while in lighter shades we show astrophysical constraints (see respective section of Sec. IV for descriptions).^a We see that in all cases, ferromagnets can be the strongest laboratory probe of ultralight DM across a broad range of masses, and in some cases can even surpass astrophysical constraints.

^a Several of these limits were acquired from Refs. [66, 67]. See also Refs. [58, 68–70] for other limits in this mass range which are not shown here, and Ref. [54] for a brief discussion of the caveats regarding those limits.

V. CONCLUSION

In this work, we determined the sensitivity of levitated ferromagnets to AC magnetic fields and to various ultra-light DM candidates. In the presence of an applied magnetic field, a ferromagnet may either precess around the applied field (similar to an electron spin) or librate in the plane of the applied field (similar to a compass needle). While the distinction between these behaviors has been studied for DC magnetic fields, the cases when precession v.s. libration occurs in the presence of an AC magnetic field has not been adequately studied. In this work, we determined the response of a ferromagnet to an AC magnetic field as a function of frequency, paying special attention to the presence of any trapping potential used to levitate the ferromagnet. We determined three possible cases for the behavior of the system: a “trapped” case, where the trapping potential is strong in both directions so that only libration occurs; a “partially trapped” case, where the ferromagnet is only trapped strongly in one direction, so precession is possible in one direction within a certain frequency range; and a “gyroscope” case, where the ferromagnet is weakly trapped, so that precession can occur in both directions within a certain frequency range.

We then computed the magnetic-field sensitivity of various ferromagnet setups, using the formalism of Sec. II to account for motion in both angular modes. We considered three possible setups: one representative of an existing levitated setup [5] (but with an additional readout for the θ -mode), a future levitated setup, and a space-based freefall setup comparable to LISA Pathfinder. All three setups manifest the “trapped” behavior. In Eq. (60), we show the optimal range for the readout coupling. This range comes from demanding that thermal noise dominates over imprecision and back-action noise at low frequencies. (This is only possible when Eq. (57) is met; see Sec. III A for optimal choices when this condition is not met.) Both modes of the existing setup do not fall in the range in Eq. (60), and so are under-coupled. The other two lie in the range in Eq. (60), but the freefall setup could benefit from an even stronger coupling, which would improve its sensitivity at high frequencies. We also note that the freefall setup could be further improved if the system can be lowered to cryogenic temperatures and ultrahigh vacuum, similar to Gravity Probe B [7, 71].

Finally, we use the results of Sec. III to determine the sensitivity of these setups to various DM candidates. We consider sensitivity to an axion-electron coupling, a dark-photon kinetic mixing, and an axion-photon coupling. While many experiments which detect magnetic fields have sensitivity to either an axion-electron coupling [21] or to a kinetic mixing and an axion-photon coupling [29, 53, 56, 62], levitated ferromagnets are unique in their ability to achieve good sensitivity to all three of

these potential DM couplings. In all three cases, ferromagnet setups could become the most sensitive laboratory probes of these DM candidates, and for the axion DM cases, they could surpass even the leading astrophysical constraints at low frequencies. Levitated ferromagnets may also be sensitive to gravitational waves [72]. We leave further exploration of this idea to future work. While the results of this work are already quite promising, further optimization of the setups proposed here may lead to even better detection prospects for new physics.

ACKNOWLEDGMENTS

We thank Yifan Chen, Raymond Co, Keisuke Hariyama, and Yue Zhao for their helpful discussions.

S.K. and Z.L. are supported in part by the U.S. Department of Energy, Office of Science, National Quantum Information Science Research Centers, Superconducting Quantum Materials and Systems Center (SQMS) under contract number DE-AC02-07CH11359. S.K. and Z.L. also acknowledge support from the Simons Foundation Targeted Grant 920184 to the Fine Theoretical Physics Institute, which positively impacted our work. In addition, Z.L. is supported in part by the DOE grant DE-SC0011842.

D.B., D.F.J.K., W.J., A.S., C.T., H.U., and A.V. acknowledge support from the QuantERA II Programme (project LEMAQUME) that has received funding from the European Union’s Horizon 2020 research and innovation programme under Grant Agreement No 101017733.

The work of D.F.J.K. was supported by the U.S. National Science Foundation under grant PHYS-2110388.

The work of A.O.S. was supported by the U.S. National Science Foundation CAREER grant PHY-2145162, and by the Gordon and Betty Moore Foundation, grant DOI 10.37807/gbmfl2248.

C.T. and H.U. would like to thank for support the UKRI EPSRC (EP/W007444/1, EP/V035975/1, EP/V000624/1 and EP/X009491/1), the Leverhulme Trust (RPG-2022-57), and the EU Horizon Europe EIC Pathfinder project QuCoM (10032223).

A.V. acknowledges financial support from the Italian Ministry for University and Research within the Italy-Singapore Scientific and Technological Cooperation Agreement 2023-2025.

T.W. acknowledges support from A*STAR Career Development Fund (222D800028), Italy-Singapore science and technology collaboration grant (R23I0IR042), Delta-Q (C230917004, Quantum Sensing), and Competitive Research Programme (NRF-CRP30-2023-0002).

The code used for this research is made publicly available through Github [23] under CC-BY-NC-SA.

[1] D. F. Jackson Kimball, A. O. Sushkov and D. Budker, *Precessing ferromagnetic needle magnetometer*, *Phys.*

Rev. Lett. **116** (May 2016) 190801.

[2] J. Prat-Camps, C. Teo, C. C. Rusconi, W. Wieczorek and O. Romero-Isart, *Ultrasensitive inertial and force sensors with diamagnetically levitated magnets*, *Phys. Rev. Appl.* **8** (Sep 2017) 034002.

[3] A. Vinante, P. Falferi, G. Gasbarri, A. Setter, C. Timberlake and H. Ulbricht, *Ultralow mechanical damping with meissner-levitated ferromagnetic microparticles*, *Phys. Rev. Appl.* **13** (Jun 2020) 064027.

[4] A. Vinante, C. Timberlake, D. Budker, D. F. J. Kimball, A. O. Sushkov and H. Ulbricht, *Surpassing the energy resolution limit with ferromagnetic torque sensors*, *Phys. Rev. Lett.* **127** (Aug 2021) 070801.

[5] F. Ahrens, W. Ji, D. Budker, C. Timberlake, H. Ulbricht and A. Vinante, *Levitated ferromagnetic magnetometer with energy resolution well below \hbar* , [arXiv:2401.03774](https://arxiv.org/abs/2401.03774).

[6] P. Fadeev, C. Timberlake, T. Wang, A. Vinante, Y. B. Band, D. Budker et al., *Ferromagnetic gyroscopes for tests of fundamental physics*, *Quantum Science and Technology* **6** (Feb 2021) 024006.

[7] P. Fadeev, T. Wang, Y. B. Band, D. Budker, P. W. Graham, A. O. Sushkov et al., *Gravity probe spin: Prospects for measuring general-relativistic precession of intrinsic spin using a ferromagnetic gyroscope*, *Phys. Rev. D* **103** (Feb 2021) 044056.

[8] T. Wang, S. Lourette, S. R. O’Kelley, M. Kayci, Y. Band, D. F. J. Kimball et al., *Dynamics of a ferromagnetic particle levitated over a superconductor*, *Phys. Rev. Appl.* **11** (Apr 2019) 044041.

[9] R. Peccei and H. R. Quinn, *CP Conservation in the Presence of Instantons*, *Phys. Rev. Lett.* **38** (1977) 1440–1443.

[10] S. Weinberg, *A New Light Boson?*, *Phys. Rev. Lett.* **40** (1978) 223–226.

[11] F. Wilczek, *Problem of Strong P and T Invariance in the Presence of Instantons*, *Phys. Rev. Lett.* **40** (1978) 279–282.

[12] J. Preskill, M. B. Wise and F. Wilczek, *Cosmology of the Invisible Axion*, *Phys. Lett. B* **120** (1983) 127–132.

[13] L. Abbott and P. Sikivie, *A Cosmological Bound on the Invisible Axion*, *Phys. Lett. B* **120** (1983) 133–136.

[14] M. Dine and W. Fischler, *The Not So Harmless Axion*, *Phys. Lett. B* **120** (1983) 137–141.

[15] A. E. Nelson and J. Scholtz, *Dark Light, Dark Matter and the Misalignment Mechanism*, *Phys. Rev. D* **84** (2011) 103501 [[arXiv:1105.2812](https://arxiv.org/abs/1105.2812)].

[16] P. W. Graham, J. Mardon and S. Rajendran, *Vector Dark Matter from Inflationary Fluctuations*, *Phys. Rev. D* **93** (2016) 103520 [[arXiv:1504.02102](https://arxiv.org/abs/1504.02102)].

[17] D. Antypas et al., *New Horizons: Scalar and Vector Ultralight Dark Matter*, [arXiv:2203.14915](https://arxiv.org/abs/2203.14915).

[18] P. Arias, D. Cadamuro, M. Goodsell, J. Jaeckel, J. Redondo and A. Ringwald, *WISPy Cold Dark Matter*, *JCAP* **06** (2012) 013 [[arXiv:1201.5902](https://arxiv.org/abs/1201.5902)].

[19] D. F. Jackson Kimball and K. van Bibber, *The Search for Ultralight Bosonic Dark Matter*. Springer, 2022, 10.1007/978-3-030-95852-7.

[20] W. A. Terrano, E. G. Adelberger, C. A. Hagedorn and B. R. Heckel, *Constraints on axionlike dark matter with masses down to 10^{-23} eV/c²*, *Phys. Rev. Lett.* **122** (Jun 2019) 231301.

[21] J. Lee, M. Lisanti, W. A. Terrano and M. Romalis, *Laboratory constraints on the neutron-spin coupling of few-scale axions*, *Phys. Rev. X* **13** (Mar 2023) 011050.

[22] QUAX COLLABORATION, N. Crescini, D. Alesini, C. Braggio, G. Carugno, D. D’Agostino, D. Di Gioacchino et al., *Axion search with a quantum-limited ferromagnetic haloscope*, *Phys. Rev. Lett.* **124** (May 2020) 171801.

[23] <https://github.com/skalia618/LevitatedFerromagnets>.

[24] S. M. Bhagat and P. Lubitz, *Temperature variation of ferromagnetic relaxation in the 3d transition metals*, *Phys. Rev. B* **10** (Jul 1974) 179–185.

[25] Y. B. Band, Y. Avishai and A. Shnirman, *Dynamics of a magnetic needle magnetometer: Sensitivity to landau-lifshitz-gilbert damping*, *Phys. Rev. Lett.* **121** (Oct 2018) 160801.

[26] S. Earnshaw, *On the nature of the molecular forces which regulate the constitution of the luminiferous ether*, *Transactions of the Cambridge Philosophical Society* **7** (1842) 97–112.

[27] F. Moon and P. Chang, *Superconducting Levitation: Applications to Bearing & Magnetic Transportation*. Wiley VCH, 2004.

[28] A. Einstein and W. J. de Haas, *Experimenteller Nachweis der Ampereschen Molekularströme*, *Deutsche Physikalische Gesellschaft, Verhandlungen* **17** (1915) 152–170.

[29] G. Higgins, S. Kalia and Z. Liu, *Maglev for dark matter: Dark-photon and axion dark matter sensing with levitated superconductors*, *Phys. Rev. D* **109** (Mar 2024) 055024.

[30] R. F. Voss, *Uncertainty principle limit to the energy sensitivity of SQUID’s and other linear amplifiers*, *Applied Physics Letters* **38** (02 1981) 182–184.

[31] J. Gieseler, A. Kabcenell, E. Rosenfeld, J. Schaefer, M. S. A. Safira, C. Gonzalez-Ballester et al., *Single-spin magnetomechanics with levitated micromagnets*, *Phys. Rev. Lett.* **124** (2020) 163604.

[32] T. Fuchs, D. G. Uitenbroek, J. Plugge, N. V. Halteren, J.-P. V. Soest, A. Vinante et al., *Measuring gravity with milligram levitated masses*, *Science Advances* **10** (2024) adk2949.

[33] L. Dania, D. S. Bykov, F. Goschin, M. Teller, A. Kassid and T. E. Northup, *Ultrahigh quality factor of a levitated nanomechanical oscillator*, *Physical Review Letters* **132** (2024) 133602.

[34] LISA PATHFINDER COLLABORATION, M. Armano, H. Audley, J. Baird, M. Bassan, P. Binetruy, M. Born et al., *Nano-newton electrostatic force actuators for femto-newton-sensitive measurements: System performance test in the LISA pathfinder mission*, *Phys. Rev. D* **109** (May 2024) 102009.

[35] M. Armano, H. Audley, J. Baird, P. Binetruy, M. Born, D. Bortoluzzi et al., *Beyond the required LISA free-fall performance: New LISA pathfinder results down to 20 μHz*, *Phys. Rev. Lett.* **120** (Feb 2018) 061101.

[36] THE NEDM COLLABORATION AT PSI, N. J. Ayres, G. Ban, G. Bison, K. Bodek, V. Bondar, T. Bouillaud et al., *Achieving ultra-low and -uniform residual magnetic fields in a very large magnetically shielded room for fundamental physics experiments*, *Eur. Phys. J. C* **84** (Jan 2024) .

[37] D. Budker and M. Romalis, *Optical magnetometry*, *Nature Physics* **3** (2007) 227–234.

[38] D. Budker and D. Kimball, *Optical Magnetometry*. Cambridge University Press, 2013.

[39] P. Nguyen, R. M. S. Schofield, A. Effler, C. Austin, V. Adya, M. Ball et al., *Environmental noise in advanced ligo detectors*, *Classical and Quantum Gravity* **38** (June 2021) 145001.

[40] S. Sendelbach, *Investigations of 1/f flux noise in superconducting quantum circuits*. PhD thesis, University of Wisconsin – Madison, 2013.

[41] C. Cinquegrana, E. Majorana, P. Rapagnani and F. Ricci, *Back-action-evasive transducing scheme for cryogenic gravitational wave antennas*, *Phys. Rev. D* **48** (Jul 1993) 448–465.

[42] H. J. Paik, C. E. Griggs, M. V. Moody, K. Venkateswara, H. M. Lee, A. B. Nielsen et al., *Low-frequency terrestrial tensor gravitational-wave detector*, *Classical and Quantum Gravity* **33** (Mar 2016) 075003.

[43] H. J. Paik, *Superconducting inductance-bridge transducer for resonant-mass gravitational-radiation detector*, *Phys. Rev. D* **33** (Jan 1986) 309–318.

[44] N. W. Evans, C. A. J. O’Hare and C. McCabe, *Refinement of the standard halo model for dark matter searches in light of the Gaia Sausage*, *Phys. Rev. D* **99** (2019) 023012 [[arXiv:1810.11468](https://arxiv.org/abs/1810.11468)].

[45] J. W. Foster, N. L. Rodd and B. R. Safdi, *Revealing the dark matter halo with axion direct detection*, *Physical Review D* **97** (June 2018) .

[46] G. P. Centers, J. W. Blanchard, J. Conrad, N. L. Figueroa, A. Garcon, A. V. Gramolin et al., *Stochastic fluctuations of bosonic dark matter*, *Nat. Comm.* **12** (2021) 7321.

[47] M. Lisanti, M. Moschella and W. Terrano, *Stochastic properties of ultralight scalar field gradients*, *Physical Review D* **104** (Sept. 2021) .

[48] N. Blinov, C. Gao, R. Harnik, R. Janish and N. Sinclair, *Dark Matter Searches on a Photonic Chip*, [arXiv:2401.17260](https://arxiv.org/abs/2401.17260).

[49] D. Y. Cheong, N. L. Rodd and L.-T. Wang, *A Quantum Description of Wave Dark Matter*, [arXiv:2408.04696](https://arxiv.org/abs/2408.04696).

[50] W. A. Terrano, E. G. Adelberger, J. G. Lee and B. R. Heckel, *Short-range spin-dependent interactions of electrons: a probe for exotic pseudo-goldstone bosons*, [arXiv:1508.02463](https://arxiv.org/abs/1508.02463).

[51] E. Aprile, K. Abe, F. Agostini, S. Ahmed Maouloud, L. Althueser, B. Andrieu et al., *Search for new physics in electronic recoil data from xenonnt*, *Physical Review Letters* **129** (Oct. 2022) .

[52] F. Capozzi and G. Raffelt, *Axion and neutrino bounds improved with new calibrations of the tip of the red-giant branch using geometric distance determinations*, *Physical Review D* **102** (Oct. 2020) .

[53] M. A. Fedderke, P. W. Graham, D. F. Jackson Kimball and S. Kalia, *Earth as a transducer for dark-photon dark-matter detection*, *Physical Review D* **104** (Oct. 2021) .

[54] I. M. Bloch and S. Kalia, *Curl up with a good b: detecting ultralight dark matter with differential magnetometry*, *Journal of High Energy Physics* **2024** (Jan. 2024) .

[55] M. A. Fedderke, P. W. Graham, D. F. Jackson Kimball and S. Kalia, *Search for dark-photon dark matter in the SuperMAG geomagnetic field dataset*, *Phys. Rev. D* **104** (2021) 095032 [[arXiv:2108.08852](https://arxiv.org/abs/2108.08852)].

[56] I. A. Sulai, S. Kalia, A. Arza, I. M. Bloch, E. C. Muñoz, C. Fabian et al., *Hunt for magnetic signatures of hidden-photon and axion dark matter in the wilderness*, *Phys. Rev. D* **108** (Nov 2023) 096026.

[57] M. Jiang, T. Hong, D. Hu, Y. Chen, F. Yang, T. Hu et al., *Search for dark photons with synchronized quantum sensor network*, [arXiv:2305.00890](https://arxiv.org/abs/2305.00890).

[58] A. Caputo, H. Liu, S. Mishra-Sharma and J. T. Rudereman, *Dark photon oscillations in our inhomogeneous universe*, *Phys. Rev. Lett.* **125** (2020) 221303 [[arXiv:2002.05165](https://arxiv.org/abs/2002.05165)].

[59] D. Wadekar and G. R. Farrar, *Gas-rich dwarf galaxies as a new probe of dark matter interactions with ordinary matter*, *Phys. Rev. D* **103** (2021) 123028 [[arXiv:1903.12190v3](https://arxiv.org/abs/1903.12190v3)].

[60] S. D. McDermott and S. J. Witte, *Cosmological evolution of light dark photon dark matter*, *Phys. Rev. D* **101** (2020) 063030 [[arXiv:1911.05086](https://arxiv.org/abs/1911.05086)].

[61] A. V. Gramolin, D. Aybas, D. Johnson, J. Adam and A. O. Sushkov, *Search for axion-like dark matter with ferromagnets*, *Nature Physics* **17** (2021) 79–84.

[62] A. Arza, M. A. Fedderke, P. W. Graham, D. F. Jackson Kimball and S. Kalia, *Earth as a transducer for axion dark-matter detection*, *Phys. Rev. D* **105** (May 2022) 095007 [[arXiv:2112.09620](https://arxiv.org/abs/2112.09620)].

[63] CAST, V. Anastassopoulos, S. Aune, K. Barth, A. Belov, H. Bräuninger, G. Cantatore et al., *New CAST limit on the axion-photon interaction*, *Nature Physics* **13** (2017) 584–590 [[arXiv:1705.02290](https://arxiv.org/abs/1705.02290)].

[64] S. Hoof and L. Schulz, *Updated constraints on axion-like particles from temporal information in supernova SN1987A gamma-ray data*, *Journal of Cosmology and Astroparticle Physics* **2023** (Mar 2023) 054.

[65] J. Sisk-Reynés, J. H. Matthews, C. S. Reynolds, H. R. Russell, R. N. Smith and M. C. D. Marsh, *New constraints on light axion-like particles using Chandra transmission grating spectroscopy of the powerful cluster-hosted quasar H1821+643*, *Monthly Notices of the Royal Astronomical Society* **510** (12 2021) 1264–1277.

[66] <https://cajohare.github.io/AxionLimits/> (accessed 2023).

[67] A. Caputo, A. J. Millar, C. A. O’Hare and E. Vitagliano, *Dark photon limits: A handbook*, *Physical Review D* **104** (Nov 2021) .

[68] V. Cardoso, O . J. Dias, G. S. Hartnett, M. Middleton, P. Pani and J. E. Santos, *Constraining the mass of dark photons and axion-like particles through black-hole superradiance*, *Journal of Cosmology and Astroparticle Physics* **2018** (Mar 2018) 043–043.

[69] S. J. Witte, S. Rosauro-Alcaraz, S. D. McDermott and V. Poulin, *Dark photon dark matter in the presence of inhomogeneous structure*, *JHEP* **06** (2020) 132 [[arXiv:2003.13698](https://arxiv.org/abs/2003.13698)].

[70] M. Escudero, C. K. Pooni, M. Fairbairn, D. Blas, X. Du and D. J. E. Marsh, *Axion star explosions: A new source for axion indirect detection*, [arXiv:2302.10206](https://arxiv.org/abs/2302.10206).

[71] C. W. F. Everitt, D. B. DeBra, B. W. Parkinson, J. P. Turneaure, J. W. Conklin, M. I. Heifetz et al., *Gravity probe b: Final results of a space experiment to test general relativity*, *Phys. Rev. Lett.* **106** (May 2011) 221101.

[72] D. Carney, G. Higgins, G. Marocco and M. Wentzel, *A Superconducting Levitated Detector of Gravitational Waves*, [arXiv:2408.01583](https://arxiv.org/abs/2408.01583).

[73] S. Chaudhuri, P. W. Graham, K. Irwin, J. Mardon, S. Rajendran and Y. Zhao, *Radio for hidden-photon dark matter detection*, *Phys. Rev. D* **92** (2015) 075012 [[arXiv:1411.7382](https://arxiv.org/abs/1411.7382)].

Appendix A: Signal-to-noise ratio

In this appendix, we derive an appropriate SNR for our system. Defining such an SNR is complicated by the fact that we have sensitivity to magnetic fields in two directions, so in this appendix, we pay special attention to the matrix nature of our noise $S_{BB}^{\text{tot}}(\omega)$. Here, we consider sensitivity to an AC magnetic field signal¹⁸

$$\mathbf{B}_S(t) = \left(B_{S,n} \hat{\mathbf{n}}_0 + B_{S,\theta} \hat{\theta}_0 + B_{S,\phi} \hat{\phi}_0 \right) \cos(\omega_S t + \Phi_S) \quad (\text{A-1})$$

of unknown direction and phase. (As we are insensitive to the $\hat{\mathbf{n}}_0$ direction, we will ignore $B_{S,n}$.) We will take the distribution of \mathbf{B}_S to be Gaussian and isotropic so that each component follows an independent Gaussian distribution with mean zero and $\langle B_{S,\alpha}^2 \rangle = \bar{B}_S^2/3$ (where $\langle \cdot \rangle$ represents an ensemble-average). Meanwhile, the noise $\mathbf{B}_N(t)$ has a Fourier transform whose components satisfy

$$\langle \tilde{B}_{N,\alpha}(\omega) \tilde{B}_{N,\beta}(\omega)^* \rangle = \frac{S_{BB,\alpha\beta}^{\text{tot}}(\omega) t_{\text{int}}}{2}, \quad (\text{A-2})$$

where t_{int} is the integration time of the experiment (and $\tilde{\mathbf{B}}_N$ is uncorrelated at different frequencies).

When we perform an experiment, we measure the Fourier transform of the total magnetic field $\tilde{\mathbf{B}}_{\text{tot}} = \tilde{\mathbf{B}}_S + \tilde{\mathbf{B}}_N$, if there exists a signal, or simply $\tilde{\mathbf{B}}_{\text{tot}} = \tilde{\mathbf{B}}_N$, if there does not. To distinguish these two scenarios, we ought to combine the information from the different components of $\tilde{\mathbf{B}}_{\text{tot}}$ (for a fixed frequency) into a single test statistic

$$q = \tilde{\mathbf{B}}_{\text{tot}}^\dagger X \tilde{\mathbf{B}}_{\text{tot}}, \quad (\text{A-3})$$

for some Hermitian matrix X to be chosen momentarily. In the scenario where there is no signal, this statistic has

$$\langle q \rangle_0 = \langle \tilde{\mathbf{B}}_N^\dagger X \tilde{\mathbf{B}}_N \rangle = \text{Tr} [X \langle \tilde{\mathbf{B}}_N \tilde{\mathbf{B}}_N^\dagger \rangle] \quad (\text{A-4})$$

$$= \frac{t_{\text{int}}}{2} \text{Tr} [X S_{BB}^{\text{tot}}], \quad (\text{A-5})$$

$$\langle q^2 \rangle_0 = \langle \tilde{\mathbf{B}}_N^\dagger X \tilde{\mathbf{B}}_N \tilde{\mathbf{B}}_N^\dagger X \tilde{\mathbf{B}}_N \rangle \quad (\text{A-6})$$

$$= \frac{t_{\text{int}}^2}{4} \left(\text{Tr} [X S_{BB}^{\text{tot}}]^2 + \text{Tr} [X S_{BB}^{\text{tot}} X S_{BB}^{\text{tot}}] \right). \quad (\text{A-7})$$

¹⁸ This would be the form of the signal in the case of an axion-electron coupling. In the case of a DPDM kinetic mixing, each term in Eq. (A-1) would have its own phase Φ_S [see also Eq. (74)]. This has no impact on the rest of the calculation in this appendix. In the case of an axion-photon coupling, the direction of the signal is, in principle, not random but rather can be predicted through a sufficiently accurate signal calculation. As we do not perform such a calculation in this work, we treat the direction as random in our sensitivity projections, and so the formalism of this appendix still applies.

On the other hand, when a signal is present, its expectation is

$$\langle q \rangle_S = \langle \tilde{\mathbf{B}}_S^\dagger X \tilde{\mathbf{B}}_S \rangle + \langle \tilde{\mathbf{B}}_N^\dagger X \tilde{\mathbf{B}}_N \rangle \quad (\text{A-8})$$

$$= \frac{\bar{B}_S^2 t_{\text{int}}^2}{12} \text{Tr} [X] + \frac{t_{\text{int}}}{2} \text{Tr} [X S_{BB}^{\text{tot}}]. \quad (\text{A-9})$$

A signal is distinguishable when the difference between q with/without the signal exceeds the standard deviation of q without any signal. That is, we should define the SNR as

$$\text{SNR} = \frac{\langle q \rangle_S - \langle q \rangle_0}{\sqrt{\langle q^2 \rangle_0 - \langle q \rangle_0^2}} \quad (\text{A-10})$$

$$= \frac{\bar{B}_S^2 t_{\text{int}} \text{Tr} [X]}{6 \sqrt{\text{Tr} [X S_{BB}^{\text{tot}} X S_{BB}^{\text{tot}}]}}. \quad (\text{A-11})$$

Now we can consider what an optimal choice of X would be. The only matrix structure available is S_{BB}^{tot} , and so we should choose $X \propto (S_{BB}^{\text{tot}})^n$ for some n . If S_{BB}^{tot} has two eigenvalues λ_1, λ_2 , then this becomes

$$\text{SNR} = \frac{\bar{B}_S^2 t_{\text{int}} (\lambda_1^n + \lambda_2^n)}{6 \sqrt{\lambda_1^{2n+2} + \lambda_2^{2n+2}}}. \quad (\text{A-12})$$

It is not difficult to show that this expression is maximized for $n = -2$, leading to an optimal SNR of

$$\text{SNR} = \frac{\bar{B}_S^2 t_{\text{int}}}{6} \sqrt{\lambda_1^{-2} + \lambda_2^{-2}} \quad (\text{A-13})$$

$$= \frac{\bar{B}_S^2 t_{\text{int}}}{6} \sqrt{\text{Tr} [(S_{BB}^{\text{tot}})^{-2}]} \quad (\text{A-14})$$

This can be equivalently phrased as computing the two SNRs representing the sensitivity along each eigenvector, and then summing them in quadrature.

Finally, we note that the above discussion applies when the signal is entirely coherent throughout the duration of the experiment. If the coherence time of the signal is shorter than the duration of the experiment, then we can consider each coherence time as an independent experiment. In this case, the SNRs for the individual experiments can be summed in quadrature, so that the total SNR is

$$\text{SNR} = \frac{\bar{B}_S^2 t_{\text{coh}}}{6} \sqrt{\text{Tr} [(S_{BB}^{\text{tot}})^{-2}]} \cdot \sqrt{\frac{t_{\text{int}}}{t_{\text{coh}}}}. \quad (\text{A-15})$$

Appendix B: Axion-photon coupling signal

In this appendix, we estimate the magnetic-field signal $\mathbf{B}_{a\gamma}$ induced by axion DM which couples to photons. This computation largely follows Appendix B of Ref. [29], but the background magnetic field \mathbf{B}_0 in this case will be sourced by a magnetic dipole (the ferromagnet) instead

of a pair of anti-Helmholtz coils. The axion DM signal is given by [29, 73]

$$\mathbf{B}_{a\gamma}(\mathbf{r}) = \sum_n c_n \frac{f_n}{f_a} \mathbf{B}_n(\mathbf{r}) e^{-im_a t}, \quad (\text{B-1})$$

$$c_n = -\frac{\sqrt{\hbar c^3} g_{a\gamma} f_a^2 a_0}{f_n^2 - f_a^2} \int dV \mathbf{E}_n(\mathbf{r})^* \cdot \mathbf{B}_0(\mathbf{r}), \quad (\text{B-2})$$

where \mathbf{E}_n and \mathbf{B}_n are the electric/magnetic fields for the cavity modes of the shield (which have corresponding frequencies f_n and are normalized so that $\int dV |\mathbf{E}_n|^2 = 1$).

In order to estimate the overlap integral in Eq. (B-2), it is useful to write \mathbf{B}_0 as the gradient of a magnetic potential, which is possible in the absence of free currents or magnetization (for static magnetic fields). Of course, the ferromagnet is magnetized, so \mathbf{B}_0 itself cannot be written this way. However because there are no free currents, we may write $\mathbf{B}_0 = \mu_0(\mathbf{H}_0 + \mathbf{M})$ with $\nabla \times \mathbf{H}_0 = 0$. Because \mathbf{H}_0 is curl-free, it can be written as $\mathbf{H}_0 = \nabla \Psi_0$. Then the overlap integral becomes

$$\int dV \mathbf{E}_n^* \cdot \mathbf{B}_0 = \mu_0 \left(\int dA \cdot \mathbf{E}_n \Psi_0 + \int dV \mathbf{E}_n^* \cdot \mathbf{M} \right). \quad (\text{B-3})$$

The second integral in Eq. (B-3) only has support over the volume of the ferromagnet. Assuming that the ferromagnet is much smaller than the size of the shield, \mathbf{E}_n will be roughly constant over this volume, and so we can

approximate this integral as $\mu_0 \mathbf{E}_n^* \cdot \boldsymbol{\mu}$, where $\boldsymbol{\mu}$ is the magnetic moment of the ferromagnet.

To compute the first integral in Eq. (B-3) requires an exact expression for Ψ_0 on the boundary of the shield. In the absence of the shield, this is just a magnetic dipole. However, if the shield is superconducting, then \mathbf{B}_0 will be modified in order to ensure that the perpendicular magnetic field vanishes at the boundary of the shield. As in Sec. II A, this can be accounted for via the method of images. As we only wish to derive a parametric estimate for the axion DM signal, we will simply take the magnetic potential of a dipole

$$\Psi_0(\mathbf{r}) = \frac{\boldsymbol{\mu} \cdot (\mathbf{r} - \mathbf{r}_0)}{4\pi|\mathbf{r} - \mathbf{r}_0|^3}, \quad (\text{B-4})$$

where \mathbf{r}_0 is the location of the ferromagnet. Parametrically, the first integral in Eq. (B-3) is then also $\sim \mu_0 \mathbf{E}_n^* \cdot \boldsymbol{\mu}$.

Since $E_n, B_n \sim L^{-3/2}$ and $f_n \sim \frac{c}{L} \gg f_a$, then parametrically Eq. (B-1) becomes

$$B_{a\gamma} \sim \frac{\sqrt{\hbar c^3} g_{a\gamma} f_a a_0}{f_n} \cdot \mu_0 E_n \boldsymbol{\mu} \cdot \mathbf{B}_n \quad (\text{B-5})$$

$$\sim \sqrt{2\hbar c \rho_{\text{DM}}} \mu_0 \frac{g_{a\gamma} \boldsymbol{\mu}}{L^2}. \quad (\text{B-6})$$

In principle, the overlap integrals in Eq. (B-3) can be computed for each mode, and they can be summed to determine the exact proportionality constant in Eq. (B-6). Numerically, we find that this sum exhibits poor convergence, and so we remain content with a parametric estimate. (In Eq. (81), we include a conservative $\mathcal{O}(0.1)$ factor, in line with the factor computed in Ref. [29].) In future work, detailed finite element method calculations may be necessary to predict an accurate axion DM signal.